Stellar Cycles in Fully Convective Stars and a New Interpretation of Dynamo Evolution

Zackery A. Irving[1,2], Steven H. Saar[2] , Bradford J. Wargelin[2] , and José-Dias do Nascimento, Jr[2,3]

[1] School of Physics and Astronomy, University of Southampton, University Road, Southampton SO17 1BJ, UK; zi1g18@soton.ac.uk
[2] Center for Astrophysics|Harvard & Smithsonian, 60 Garden Street, Cambridge, MA 02138, USA
[3] Univ. Federal do Rio G. do Norte, UFRN, Dep. de Física, CP 1641, 59072-970, Natal, RN, Brazil

Abstract

An $\alpha\Omega$ dynamo, combining shear and cyclonic convection in the tachocline, is believed to generate the solar cycle. However, this model cannot explain cycles in fast rotators (with minimal shear) or in fully convective stars (no tachocline); an analysis of these stars could therefore provide key insights into how these cycles work. We reexamine ASAS data for 15 M dwarfs, 11 of which are presumed fully convective; the addition of newer ASAS-SN data confirms cycles in roughly 12 of them, while presenting new or revised rotation periods for 5 stars. The amplitudes and periods of these cycles follow $A_{\rm cyc} \propto P_{\rm cyc}^{0.94\pm0.11}$, with $P_{\rm cyc}/P_{\rm rot} \propto Ro^{-1.02\pm0.06}$ (where Ro is the Rossby number), very similar to $P_{\rm cyc}/P_{\rm rot} \propto Ro^{-0.81\pm0.17}$ that we find for 40 previously studied FGK stars, although $P_{\rm cyc}/P_{\rm rot}$ and α are a factor of $\sim$20 smaller in the M stars. The very different $P_{\rm cyc}/P_{\rm rot}$–Ro relation seen here compared to previous work suggests that two types of dynamo, with opposite Ro dependences, operate in cool stars. Initially, a (likely α^2 or $\alpha^2\Omega$) dynamo operates throughout the convective zone in mid- to late-M and fast-rotating FGK stars, but once magnetic breaking decouples the core and convective envelope, a tachocline $\alpha\Omega$ dynamo begins and eventually dominates in older FGK stars. A change in α in the tachocline dynamo generates the fundamentally different $P_{\rm cyc}/P_{\rm rot}$–Ro relation.

Unified Astronomy Thesaurus concepts: M dwarf stars (982); Stellar activity (1580); Stellar magnetic fields (1610); Stellar rotation (1629)

Supporting material: figure sets

1. Introduction

Stellar cycles are (quasi-)periodic fluctuations in the intrinsic brightness of stars due to changing internal magnetic fields. These cycles are most clearly manifest visually by the appearance of starspots, but they are more easily observed by studying chromospheric (Ca II H and K) or coronal (X-ray) variability—both of which are more monotonically correlated with magnetic activity. Indeed, in the optical wave band, the solar cycle has an amplitude on the order of just 0.1%, while the coronal (X-ray) variability varies by a factor of $\sim$6 (Judge et al. 2003). Sunspot observations first led to the discovery of the 11 yr solar cycle almost 200 yr ago (Schwabe 1844). Over half a century later, it was realized that sunspots are a manifestation of solar magnetic activity (Hale 1908, 1913), and it is now understood that this 11 yr cycle is just one-half of the 22 yr polarity-reversal cycle (Hale et al. 1919; Babcock 1959, 1961). However, while the solar cycle has an average period of 11 yr, due to the quasiperiodic nature of stellar cycles, it is not uncommon for a given cycle to have a period between 9 and 13 yr (see, e.g., Donahue & Baliunas 1992).

Currently, stellar cycles are believed to be a result of dynamo processes (see, e.g., Parker 1955; Baliunas et al. 1995; Dikpati & Charbonneau 1999; Kitchatinov & Rüdiger 1999). A dynamo process is a physical mechanism in which kinetic energy is converted into magnetic energy via inductive effects of motions in an electrically conducting fluid, in a self-regenerating process. The solar cycle can be well described by an $\alpha\Omega$ dynamo, where shearing (due to differential rotation) transforms a poloidal field into a toroidal one (Ω effect), and cyclonic convection (due to Coriolis and magnetic forces) then restores the poloidal field with reversed polarity (α effect; Parker 1955; Babcock 1961; Leighton 1969). Comparing our Sun's cycle to the cycles of 4454 cool stars, Boro Saikia et al. (2018) found that the solar dynamo cycle is not uncommon. Many of the finer details of these dynamo processes, however, remain poorly understood—even in the case of our Sun (see, e.g., Ossendrijver 2003; Charbonneau 2010).

Differential rotation (DR) is a key component of the solar $\alpha\Omega$ dynamo model, with current models suggesting that the Ω effect takes place in the tachocline layer at the base of the convective envelope (e.g., Gilman & Fox 1997; Dikpati & Charbonneau 1999). In the case of our Sun, DR causes the equator to rotate more quickly than the poles; this is referred to as solar-like DR. Some theoretical work (e.g., Kitchatinov & Rüdiger 1999) and observations (e.g., Barnes et al. 2005) suggested that DR has little or no dependence on rotation, while other observations indicate that the two are closely tied (e.g., Donahue et al. 1996). Saar (2011) updated the work of Donahue et al. (1996) and confirmed that DR appears to scale almost linearly with rotation period, at least for relatively slow rotators. Saar (2011) further argued that the results of Barnes et al. (2005) were misleading as they included close binaries, where large tidal forces can freeze out DR and cause solid-body rotation.

For stars with very slow rotation, numerical simulations (e.g., Karak et al. 2020; Käpylä 2021) suggest that DR should be antisolar, where the poles rotate more quickly than the equator, although the point of transition from solar to antisolar DR is still debated. Antisolar DR in the classical $\alpha\Omega$ dynamo

model does not produce polarity reversal, and so these stars would not be expected to have solar-like cycles. Nonetheless, there is strong evidence that some slowly rotating stars do have cycles (see, e.g., Suárez Mascareño et al. 2016).

Whether DR depends on rotation rate or not, dynamo processes in more rapidly rotating stars are expected to differ fundamentally from those in the Sun, possessing $\alpha^2\Omega$ or even α^2 dynamos (e.g., Kitchatinov & Rüdiger 1999), where the dynamo actions originate from surface shear or in the convection zone, respectively. Kitchatinov & Rüdiger (1999) suggested that these α^2 dynamos should not result in cyclic activity, and could explain why Baliunas et al. (1995) found an absence of activity cycles in rapidly rotating young stars. However, more recent studies (e.g., Lehtinen et al. 2016; Suárez Mascareño et al. 2016) have shown that activity cycles are observed in fast- and slow-rotating stars alike. In addition, it is difficult to explain the observed increase in magnetic activity with rotation under the assumption that DR is constant (e.g., Durney et al. 1993; Saar 2011; Wright et al. 2011). It should be noted, however, that DR studies can only measure surface DR, not DR in the tachocline, and there is no guarantee that the two are the same.

A convective envelope is another key ingredient of the $\alpha\Omega$ dynamo. Convective envelopes surrounding a radiative core are a staple of cool stars earlier than type $\sim$M3.5, while late-M-type stars are believed to be fully convective (Chabrier & Baraffe 1997); as such, these stars cannot support solar-like $\alpha\Omega$ dynamos (because they have no tachocline). Instead, late-M-type stars are expected to support α^2 dynamos, which, as already discussed, are not expected to exhibit activity cycles. However, there is some evidence suggesting that α^2 dynamos may exhibit activity cycles under certain conditions (e.g., Rüdiger et al. 2003; Gastine et al. 2012; Käpylä et al. 2013). In addition to this, activity cycles have also been observed in several stars that are believed to be fully convective (see, e.g., Suárez Mascareño et al. 2016; Wargelin et al. 2017).

Interestingly, there is evidence suggesting that stellar activity cycle periods are (weakly) correlated with rotation period (see, e.g., Noyes et al. 1984; Brandenburg et al. 1998; Saar & Brandenburg 1999; Böhm-Vitense 2007; Suárez Mascareño et al. 2016; Boro Saikia et al. 2018; Wright et al. 2018)—M-type stars included. In their two paper series, Brandenburg et al. (1998) and Saar & Brandenburg (1999) found that FGK stars typically occupy one of three branches: termed the "super-active" (S), "active" (A), and "inactive" (I) branches, with our Sun residing approximately between the A and I branches. Saar & Brandenburg (1999) also found hints of a tentative fourth, "transitional" (T), branch connecting the A and S branches. Recent studies (e.g., Lehtinen et al. 2016; Distefano et al. 2017; Boro Saikia et al. 2018) have found further evidence for the existence of this T branch, while raising doubts about the A branch, which has become increasingly less clear as more cycles have been found.

To develop our understanding of the dynamo processes responsible for stellar activity cycles, active stars with a wide range of physical parameters should be observed. Active late-M-type stars are of particular interest because their cycles cannot be adequately explained by current dynamo models. Due to how intrinsically faint M stars are, however, they were underrepresented in earlier surveys (e.g., Wilson 1978; Baliunas et al. 1995). Furthermore, even in recent studies (e.g., Suárez Mascareño et al. 2016; Wright et al. 2018), rapidly rotating M stars are still poorly represented. Rapidly rotating late-M stars could be especially revealing, as their deep convective zones combined with short rotation periods may allow for unique dynamos.

Herein, we reexamine the 15 latest-type stars listed in Suárez Mascareño et al. (2016; excluding GJ 526, as discussed below), who analyzed $\sim$9 yr of ASAS-3 (Pojmanski 1997, 2002) photometric monitoring data and suggested that 13 of them, several of which are fully convective, showed evidence for cyclic activity. We use the same data and include new data from ASAS-SN (Shappee et al. 2014; Kochanek et al. 2017), approximately doubling the period of monitoring; in some cases, we also include TESS data to constrain shorter rotation periods. Note, however, that there is some uncertainty regarding the spectral types, and some stars may not be fully convective. GJ 526, for example, is listed in Suárez Mascareño et al. (2016) as M4, but as M2 in SIMBAD and Suárez Mascareño et al. (2015). Moreover, its V–K_S color (see Section 2.6) also indicates that it is earlier than M4. In any case, GJ 526 is often too bright for ASAS-SN monitoring ($g = 7.6$). A few stars may also be unresolved binary systems (see Section 2.3), further complicating spectral type determinations, but roughly 12 of our stars are almost certainly fully convective (see Section 2.4).

While photometric measurements are not as tightly correlated with magnetic activity as other metrics (e.g., chromospheric line intensities and coronal X-ray emission) and can suffer from counterbalancing effects between starspots and the surrounding faculae, they are technologically easier to make. Furthermore, there is evidence suggesting that in active, rapidly rotating stars, chromospheric emission can become saturated (e.g., Vilhu 1984), while starspot (and hence photometric) variability can continue to rise with increasing rotation (e.g., O'dell et al. 1995; Krishnamurthi et al. 1998).

In Section 2, we discuss the data used and the analysis performed to identify rotation periods and activity cycles in 15 M-type stars from their photometric time series. Results are presented in Section 3, and our interpretation of these results is provided in Section 4. Our final thoughts are then given in Section 5.

2. Method

2.1. Data Collection

ASAS-3 optical photometry data were downloaded from the ASAS All-Star Catalogue.[4] All ASAS-3 data use V-band filters, and individual measurements are ascribed one of four grades: A —best data; B—mean data; C—A and B without a measured indication; D—worst data. We opted to use only measurements with an A or B grade. For most stars in our sample, the MAG_2 (four pixel) aperture data had the least scatter and therefore the lowest empirical uncertainty; to be consistent, we therefore used this aperture for all our stars. We note, however, that the choice of aperture can sometimes have a significant effect on the inferred cycle period, and could explain (at least partly) why our results sometimes differ from those of Suárez Mascareño et al. (2016).[5] ASAS-3 has a FWHM point-spread

---

[4] http://www.astrouw.edu.pl/asas/?page=aasc
[5] We further note that the aperture columns are sometimes arranged inconsistently between different stars, and so care needs to be taken to ensure the same aperture is being used for all stars.

function (PSF) of typically 23″, corresponding to approximately 1.5 pixels.

ASAS-SN optical photometry data were collected using the light-curve server.[6] Early ASAS-SN data were gathered using *V*-band filters, while the most recent data use *g* band. The ASAS-SN light-curve server does not perform proper-motion corrections, unlike the ASAS All-Star Catalogue, so proper-motion-corrected coordinates had to be specified for each query. ASAS-SN has a 16″ FWHM PSF, so we allowed for a proper motion of up to 1″ either side of the input coordinates; extractions use a two pixel (16″) aperture. We then compiled these proper-motion-corrected light curves into single light curves for each star once we had downloaded all available data.

TESS optical photometry data were downloaded using the LIGHTKURVE Python package (Astropy Collaboration et al. 2018; Lightkurve Collaboration et al. 2018; Brasseur et al. 2019; Ginsburg et al. 2019), which accesses publicly available data directly from the Mikulski Archive for Space Telescopes (MAST). Only data products produced via their Science Processing Operations Center Science Analysis Pipeline (Jenkins et al. 2016) were used. For each star, we also used the pipeline aperture.

2.2. Data Preparation

2.2.1. ASAS-SN

Initially, the early *V*-band and recent *g*-band data were disjointed in the compiled ASAS-SN light curves. We therefore needed to color-correct these data. Using the empirical UBVR-uvgr relation found by Kent (1985) and improved by Windhorst et al. (1991), we can convert from *V*- into *g*-band magnitudes using

$$V = g - 0.03 - 0.42(g - r), \tag{1}$$

where *V* is the *V*-band magnitude, g is the *g*-band magnitude, and $g - r$ is the g–r color index, given by

$$g - r = 1.02(B - V) - 0.22, \tag{2}$$

where $B - V$ is the $B - V$ color index. However, M stars are relatively cool objects and emit mostly toward the red end of the optical spectrum; as such, the $B - V$ color index is not the best diagnostic for these stars. In addition, the relation given in Equation (1) was derived using predominantly O–K stars. After color-correcting *V*-band data using these formulae, residual offsets were therefore required. These offsets were computed by comparing the means of overlapping g- and *V*-band data.

Further internal cross-calibration is then required because ASAS-SN data are collected using multiple telescopes positioned around the world, with small but sometimes significant differences between nominally identical instruments. The ASAS-SN pipeline automatically adjusts for these differences, but color-dependent residuals may remain, as we found for our reddish M stars.

To correct for differences between different ASAS-SN telescopes, we first selected the telescope with the largest number of measurements, thus defining our reference data set. We then calibrated the remaining telescopes sequentially in descending order of relative overlap. To calibrate a telescope, we applied an offset such that the averages of overlapping data points between the telescope and the reference data set were

equal. Once a telescope had been calibrated, it then became part of the reference data set for subsequent calibrations. Fortunately, we did not find any instances of telescopes with no overlapping data. However, if a particular telescope was found to show unusual behavior within a given light curve (relative to the other telescopes) then this telescope's data were removed. For example, telescope "bA" showed an unusually large scatter for GJ 447, obscuring its cyclic modulations, but appeared perfectly normal for GJ 581, GJ 729, and GJ 849; this telescope's measurements were therefore removed in the former case, but kept in the latter three.

2.2.2. TESS

Uncorrected TESS light curves are dominated by scattered-light background caused by spacecraft motions. To reduce this background, we used LIGHTKURVE to perform pixel-level decorrelation (PLD), which has been shown to be effective at removing systematic noise from both Spitzer (Deming et al. 2015) and K2 (Luger et al. 2016, 2018) data. PLD works by creating masks of the object of interest and the surrounding background, and then using linear regression to model trends in the background. After subtracting this noise model from the uncorrected light curve, systematic noise is greatly reduced.

2.2.3. Outlier Removal

After performing the analysis described above on ASAS-SN and TESS data, we then removed outliers from all our data sets. For ASAS-3 data, we clipped each observing season to remove measurements more than two standard deviations from the mean.

For ASAS-SN data, we initially separated the data by telescope (and consequently, by filter). We then binned each filter's telescope-separated data according to the star's rotation period (because observing seasons were not always well defined when data were separated by telescope). ASAS-SN typically makes between one and three observations of each region of the visible sky each night (three is the nominal number); binning ASAS-SN data into bins of fewer than two days therefore becomes volatile and unreliable due to the small number of data points per bin. Consequently, we chose to bin stars with rotation periods shorter than 24 days differently, instead using bin sizes of $10P_{rot}$.[7] In all other cases, we used the rotation period. We then clipped these data using a tolerance of two standard deviations from the mean. Next, we repeated this process using bin sizes of P_{rot} if $P_{rot} \leqslant 24$ days, or $P_{rot}/12$ otherwise, with a tolerance of two and a half standard deviations from the mean (note we used a looser tolerance for these smaller bins).

After removing outliers from the telescope-separated ASAS-SN data, we recalibrated these telescopes and recorrected any residual offset between the *V*- and *g*-band data resulting from outlier removal. We then binned the entire calibrated light curve using bin sizes of P_{rot} if $P_{rot} \leqslant 24$ days, or $P_{rot}/12$ otherwise, and removed measurements more than two and a half standard deviations from the mean. In total, this usually resulted in ∼10% of the data being removed. Finally, we recalibrated these telescopes again and recorrected any residual offset between the *V*- and *g*-band data.

---

[6] https://asas-sn.osu.edu

[7] For a star with $P_{rot} = 24$ days, this is approximately equal to an observing season.

Table 1
Cycle Periods Inferred from Photometric Time Series

Star	Sp. Type	V–K_S	P_{rot} (d)	P_{rot} Lit. (d)	References	ASAS-3 P_{cyc} (yr)	ASAS-3 A_{cyc} (mmag)	Previous ASAS-3 Results P_{cyc} (yr)	Previous ASAS-3 Results A_{cyc} (mmag)	ASAS-SN P_{cyc} (yr)	ASAS-SN A_{cyc} (mmag)	Phase Match
GJ 358[a]	M3	4.638	25.2 ± 1.1	25.2 ± 0.1	2	**4.7 ± 0.9**	**21.9 ± 1.9**	4.9 ± 0.1	20.5 ± 0.9	**1.7 ± 0.2**	**10.7 ± 0.6**	poor
...	...	...	...	...	...	...	...	...	...	**3.2 ± 0.5**	**4.0 ± 0.6**	...
GJ 581	M3	4.723	141.6 ± 3.5	132.5 ± 6.3[d]	1	...	...	6.2 ± 0.9	3.8 ± 0.9	**3.8 ± 0.6**	**6.7 ± 0.6**	...
GJ 628	M3	4.997	79.6 ± 2.6	119.3 ± 0.5	2	**4.5 ± 1.3**	**8.1 ± 1.2**	4.4 ± 0.2	8.3 ± 1.1	**3.0 ± 0.5**	**5.0 ± 0.5**	good
...	...	...	...	...	...	...	...	...	...	**5.0 ± 1.2**	**3.8 ± 0.5**	...
...	...	...	...	...	...	...	...	...	...	long	...	...
GJ 849[a]	M3.5	4.772	41.4 ± 1.3	39.2 ± 6.3[d]	1	10.3 ± 3.0	25.6 ± 1.5	10.2 ± 0.9	12.4 ± 1.0	**3.7 ± 0.6**	**6.7 ± 0.5**	poor
...	...	...	...	...	...	...	...	...	...	10.8 ± 3.0	9.5 ± 0.5	...
GJ 896A[a]	M3.5	4.847	15.58 ± 0.06	15.3 ± 0.1	2	long	...	...	...	10.1 ± 2.7	8.7 ± 0.7	...
GJ 317[a]	M3.5	4.947	57.5 ± 1.7	...	...	long	...	5.2 ± 0.3	12.4 ± 1.1	**2.3 ± 0.3**	**5.7 ± 0.6**	...
...	...	...	...	...	...	...	...	...	...	10.1 ± 4.4	9.6 ± 0.6	...
GJ 273	M3.5	5.015	...	115.9 ± 19.4[d]	1	**5.8 ± 1.3**	**9.4 ± 1.2**	6.6 ± 1.3	7.7 ± 1.5	**5.9 ± 1.4**	**10.1 ± 0.8**	good
GJ 729	M3.5	5.06	2.9 ± 0.1	2.9 ± 0.1	2	**5.7 ± 1.1**	**10.4 ± 1.3**	7.1 ± 0.1	5.3 ± 0.7	**3.5 ± 1.1**	**6.8 ± 0.7**	fair
...	...	...	...	...	...	...	...	...	...	12.2 ± 6.7	8.1 ± 0.7	...
LP 816-60	M4	5.259	86.3 ± 02	67.6 ± 0.1	2	...	...	10.6 ± 1.7[g]	8.2 ± 1.2[g]	**2.0 ± 0.2**	**6.0 ± 0.8**	...
...	...	...	...	...	...	...	...	...	...	**4.2 ± 0.7**	**5.9 ± 0.6**	...
GJ 447	M4	5.499	175.9 ± 3.4	165.1 ± 0.8[f]	2	**5.3 ± 1.3**	**9.8 ± 1.4**	4.1 ± 0.3[h]	7.1 ± 1.1[h]	**5.0 ± 1.1**	**19.6 ± 1.0**	poor
...	...	...	...	...	...	...	...	...	...	10.6 ± 6.9	21.5 ± 1.0	...
GJ 285	M4	5.527	2.775 ± 0.001	2.8 ± 0.1	2	10.0 ± 4.1	39.1 ± 2.2	10.6 ± 0.4	37.2 ± 1.1	10.9 ± 4.0	37.2 ± 1.1	good
GJ 54.1	M4	5.654	71.4 ± 2.4	69.2 ± 0.1	2	...	...	...	...	**2.2 ± 0.3**	**6.8 ± 0.6**	...
...	...	...	...	...	...	...	...	...	...	**3.7 ± 0.8**	**5.8 ± 0.7**	...
...	...	...	...	...	...	...	...	...	...	long	...	...
GJ 234[b]	M4.5	5.585	1.582 ± 0.002	8.1 ± 0.1[e]	2	**5.6 ± 1.5**	**10.9 ± 1.4**	5.9 ± 0.5	10.1 ± 1.4	**5.2 ± 1.0**	**13.1 ± 0.5**	fair
GJ 551[c]	M5.5	6.75	85.1 ± 1.2	83.2 ± 0.1[d]	2	**6.7 ± 1.4**	**16.3 ± 1.5**	6.8 ± 0.3	15.5 ± 0.9	18.3 ± 14.2	39.5 ± 1.1	poor
...	...	...	...	...	...	5.1 ± 1.0[i]	20.0 ± 3.0[i]	...	...	...	...	...
...	...	...	...	...	...	long[i]	...	...	...	...	...	...
GJ 406[c]	M6	7.423	2.6 ± 0.2	...	...	13.7 ± 7.3	128.4 ± 22.4	8.9 ± 0.2	64.8 ± 1.2	12.0 ± 4.4	93.3 ± 1.1	fair

Notes. *"long"* denotes high amplitude at large P_{cyc} in a power spectrum without a well-defined peak. All cycle periods reported from this work have FAPs $\leqslant$0.1%, and likewise for previous results unless noted. Cycles highlighted in bold are deemed well defined, while all others are poorly constrained. The "Phase Match" column gives a subjective measure of how well the phases (and amplitudes) of the cycles found in this work agree where they overlap.

References. (1) Suárez Mascareño et al. (2015); (2) Suárez Mascareño et al. (2016). Previous ASAS-3 results were taken from Reference 2.
[a] Partially convective (see Section 2.4).
[b] Known binary system.
[c] Photometric monitoring may include significant contamination from physically unassociated nearby objects on the sky (see Section 2.3).
[d] FAP $\leqslant$ 0.3%.
[e] FAP = 0.3%.
[f] FAP $\leqslant$ 0.2%.
[g] FAP = 3.0%.
[h] FAP = 1.7%.
[i] From ASAS-4 data.

Since TESS data have such a high cadence, we simply binned these data into 0.1 days bins and removed outliers using a tolerance of two and a half standard deviations from the mean.

2.3. Binary Systems and Crowded Fields

When assessing our results, it is important to keep in mind that some target-star intensity extractions may suffer from contamination by binary companions or other stars that appear nearby in the sky. Winters et al. (2019) list data from an all-sky volume-limited (25pc) survey for stellar companions to 1120 M-dwarf primaries, and serves as our principal reference regarding binarity because it includes all our stars of interest except for Proxima (GJ 551). Two systems are listed as binaries: GJ 234 and GJ 896.

The GJ 234 pair has a semimajor axis of $1.''1$ (e.g., Gatewood et al. 2003; Kervella et al. 2019), but contamination by the secondary is small, with estimated intensity ratios of 100:5.3 in the B band (Gatewood et al. 2003), 100:5.9 in V (Henry et al. 1999), and 100:25 in K (Coppenbarger et al. 1994). GJ 896 A and B had a separation of $5.35''$ in 2004 (Winters et al. 2019) with an estimated V magnitude of 10.29 for component A and 2.12 mag dimmer for B (100:14 ratio). Davison et al. (2015) measured a separation of $7''$ and listed the spectral types as M3.5+M4.0. These stars are mostly blended in ASAS and ASAS-SN data, and it is difficult to determine if the lack of an obvious cycle in GJ 896A is intrinsic, from contamination by the secondary star, or variable extraction efficiencies as the pair's center of emission moves around its center of mass and proper motion.

The multiplicity of GJ 273 is somewhat unclear, with Vrijmoet et al. (2020) identifying it as a suspected double based on Gaia data, while Winters et al. (2019) conclude that the putative companion is probably an unassociated background object. Astudillo-Defru et al. (2017) analyzed HARPS RV data and report that GJ 273 has four planets, without any mention of spectral evidence for a companion; in our analysis, we treat this star as a single.

Although GJ 273, along with GJ 317 and GJ 406, were not included in their study of binarity in nearby stars using data from HIPPARCOS and Gaia DR2, Kervella et al. (2019) calculated minimum (inclination-dependent) masses for companions to the rest of the stars in our sample. Except for the two known binary systems, minimum masses were no higher than $0.25 M_J$ assuming zero inclination and orbital radii of $r = 1$ au, with mass scaling as $\sqrt{r}$. All our stars have clear rotational modulation, indicating that inclination cannot be too small (assuming rotational and orbital coplanarity), so it seems unlikely that any of the stars under study here (except for GJ 234 and GJ 896) have stellar mass companions. Many of these stars are also the subjects of radial velocity (RV) studies, which would readily reveal binarity unless the orbital inclination were very small. We particularly mention GJ 358 because of its remarkable changing cycle periods: Bonfils et al. (2013) explicitly treat this star as a single after excluding known and discovered spectroscopic binaries and visual pairs from their analysis of HARPS data.

Intensity extractions can also be affected by stars that appear nearby on the sky even if they are not physically associated. GJ 406 has a very high proper motion ($4.''72 \, \mathrm{yr}^{-1}$) and has recently passed quite close to two objects that may provide contaminating flux. Likewise, Proxima lies in a very crowded part of the sky and is currently moving at $3.''86 \, \mathrm{yr}^{-1}$ within a group of stars that, although dimmer, may be bright enough to cause significant contamination within the ASAS-3 and ASAS-SN extraction regions. These effects should be slowly varying, but they complicate interpretation of observations and may be at least partly responsible for the general brightening seen in Proxima's ASAS and ASAS-SN data.

2.4. Separating Partially from Fully Convective Stars

A further consideration to make when assessing our results is which stars are fully convective. As mentioned in Section 1, spectral type is often used to distinguish partially from fully convective M stars. However, spectral type determinations are not always a robust metric, and the boundary between subtypes is often blurred. Indeed, some of these difficulties were mentioned in Section 1 and are discussed in detail in Section 2.3. Fortunately, recent studies have alleviated some of the ambiguity in identifying fully convective M stars.

Using data from Gaia DR2, Jao et al. (2018) identified a gap in the color–magnitude diagram for the lower main sequence, which they proposed could be used to distinguish partially from fully convective M stars. van Saders & Pinsonneault (2012) first predicted this gap as the result of nonequilibrium ^{3}He fusion prior to stars becoming fully convective; using numerical simulations, Feiden et al. (2021) were able to reproduce this gap. Using this distinction, specifically in the $V–K_S$ versus M_V plane, we identify 11 of our 15 M stars as being fully convective (see Table 1). We note, however, that for a few high proper-motion stars not included in Gaia DR2, we had to use DR3 parallaxes.

2.5. Time-series Analysis Techniques

Herein, we predominantly use traditional time-series analysis techniques, specifically, Lomb–Scargle (L–S) periodograms (Lomb 1976; Scargle 1982), for two key reasons. First, more advanced techniques, such as Gaussian processes (GPs), come with a significant computational expense. Depending on the number of covariance function hyperparameters, the number of mean function parameters, the priors, and the size of the data set itself, fitting a GP model can easily take several orders of magnitude times the time it takes to obtain an L–S periodogram. Second, as we discuss below, the literature shows that stellar cycles often appear to be well approximated by sines. We note two exceptions, however: GJ 358 and GJ 551 (Proxima), whose cyclic modulations cannot adequately be described by one or two single-period sinusoids; these stars are therefore better suited to a GP analysis.

To compute the false-alarm probabilities (FAPs) on our detections, we use the approximation proposed by Baluev (2008), often referred to as the Baluev estimate. We compared this method with a more robust bootstrap simulation method for six ASAS-3 and ASAS-SN light curves, and found that results were usually within 10%, and many times within 5%; the largest difference we found was $\mathrm{FAP_{Baluev}}$: $\mathrm{FAP_{bootstrap}} \approx 0.79$.[8] Due to the computational expense of bootstrap simulations, without much improvement to performance, we prefer the Baluev estimate. In our work, we consider

---

[8] Note, however, that this result was obtained for the GJ 285 ASAS-SN light curve, where the peak in the periodogram was an order of magnitude above either method's 0.1% FAP power threshold.

an FAP of $\leqslant 0.1\%$ to constitute a significant detection; the same threshold was used in Suárez Mascareño et al. (2016).

In theory, typical time-series analysis techniques, such as fast Fourier transforms (FFTs) and L–S periodograms, may not necessarily be the best tools for the analysis of stellar cycles. Both are limited in that they model signals with sinusoids; while this may be a good model for idealized systems, it often fails in reality. Indeed, stellar cycles need not be sinusoidal in nature, nor strictly periodic.

To identify stellar cycles in unevenly sampled light curves, Olspert et al. (2018b) introduced a Bayesian generalized Lomb–Scargle periodogram with trend (BGLST); using synthetic quasiperiodic data, they showed that their BGLST performed better than the standard L–S periodogram. Moreover, in their follow-up paper, Olspert et al. (2018a) further showed that GPs can be used effectively in the analysis of stellar cycles - in their case, using Ca II H and K data.

The greatest benefit of GPs over traditional time-series analysis techniques, such as the L–S periodogram, is their flexibility. Much like L–S periodograms, GPs can be used with unevenly sampled data. However, GPs need not assume the data contain a periodic, sinusoidal signal. The assumptions of a GP are encoded in its mean and covariance functions, which, in theory, allows for any number of arbitrary assumptions to be made.

Olspert et al. (2018a), in their study of stellar cycles, compared the performance of a Bayesian harmonic (i.e., sinusoidal) regression model, and GP models with periodic and quasiperiodic covariance functions. They found that where traditional methods suggest double cycles, their quasiperiodic GP model often found only a single cycle; as the assumption of a quasiperiodic signal has more physical justifications, Olspert et al. (2018a) concluded that double cycles are rarer than initial results (e.g., Wilson 1978; Baliunas et al. 1995; Brandenburg et al. 1998; Saar & Brandenburg 1999) suggest.

However, while a quasiperiodic model is more physically justified, its results are often not much of an improvement over a simple harmonic model. Olspert et al. (2018a) identified harmonic signals in the light curves in 36 stars; quasiperiodic signals were also identified in 26 of these 36 stars. Comparing these 26 quasiperiodic periods with their harmonic equivalents, 22 were comfortably within 3σ. This suggests that while stellar cycles need not be strictly periodic nor sinusoidal, they can often be well approximated by sines.

2.6. Determining Periods

2.6.1. Rotation Periods from Photometric Time Series

To determine rotation periods, we used L–S periodograms, as well as data from both ASAS-SN and TESS. ASAS-3 data are noisier and lower cadence than ASAS-SN data, and therefore provide no additional benefit for rotational studies; for these reasons, ASAS-3 data are not included. The first step in our analysis was to separate the ASAS-SN data by observing season. We then computed L–S periodograms for each of these seasons, and, provided the period of the peak was greater than 15 days, used the tallest peak in each season's L–S periodogram to fit a sine model using the Levenberg–Marquardt (L–M) algorithm (a sophisticated nonlinear least-squares fitting algorithm; see Moré 1978)—as shown in Figure 1 for GJ 54.1. Note that there were often no significant peaks at $P_{\rm rot}/2$.

We discarded periodograms computed from seasons with low data density or incomplete seasons,[9] and identified significant peaks in each periodogram. After disregarding anomalous peaks, such as the broad peak at approximately 180 days in the third row of Figure 1, we inferred the rotation period by computing the mean period of the remaining peaks, and estimated the uncertainty as the standard deviation on this mean.

However, if the rotation period of a star was sufficiently short (shorter than 15 days), we used the higher cadence but shorter duration TESS data (TESS observation windows typically span ∼27 days) to better constrain this period. If a star had multiple TESS observations, we found that in every case, the inferred periods were identical to within the (tightly constrained) uncertainties.

Our analysis using TESS data proceeded in much the same way as our analysis using ASAS-SN data; an example is shown in Figure 2 for GJ 234. Due to our currently limited understanding of TESS systematics, however, the identification of rotation periods is restricted to below approximately half a TESS observing window (hence our 15 days cutoff)—see, for example, Anthony et al. (2022) and Claytor et al. (2022).

To infer the rotation period of a star from its TESS light curve, we fit a Gaussian to the tallest peak in its periodogram. Our estimate for the rotation period was thus the mean of this Gaussian, with the uncertainty given by its standard deviation. Since we were often limited to one or two TESS observations, following the same procedure as described above for ASAS-SN resulted in unrealistically small errors in some cases and no errors in others; we therefore adopted this alternative method. We note that when we tested this approach on ASAS-SN data, it resulted in larger uncertainties due to the broad peaks in these periodograms. However, TESS observations only span ∼27 days, and so these broadening effects (e.g., resulting from differential rotation and multiple starspot generations) are minimal. TESS is also a space-based observatory, with a much higher signal-to-noise ratio than ASAS-SN. Given these differences, we deem this alternative method to be appropriate. Results are presented in Table 1 and are discussed in Section 3.

2.6.2. Cycle Periods from Photometric Time Series

To determine cycle periods, we typically use L–S periodograms incorporating data from both ASAS-3 and ASAS-SN; exceptions to this are Proxima (for which we also have ASAS-4 data and use GPs), and GJ 358 (for which we also use GPs)—see Section 2.5 for more details.

For each star, we computed a L–S periodogram from its light curve. We then identified significant peaks in periodograms with periods of more than 1.5 yr, and used the periods of these peaks to fit sine functions to the light curve; see Figures 3 and 4 for examples. All ASAS-3/-4 light curves and associated periodograms (16 images) are provided in Figure Set 3; likewise for ASAS-SN (15 images) in Figure Set 4.

If a periodogram contained multiple significant peaks, we fit sine functions using each peak and then combined these functions to create a superposition. If the fit of the superposition was worse than the fit of any single component, then the worst fitting components were removed until the fit of the superposition was better than the fit of any single component,

---

[9] In some cases, incomplete seasons were included if multiple rotations were clearly shown.
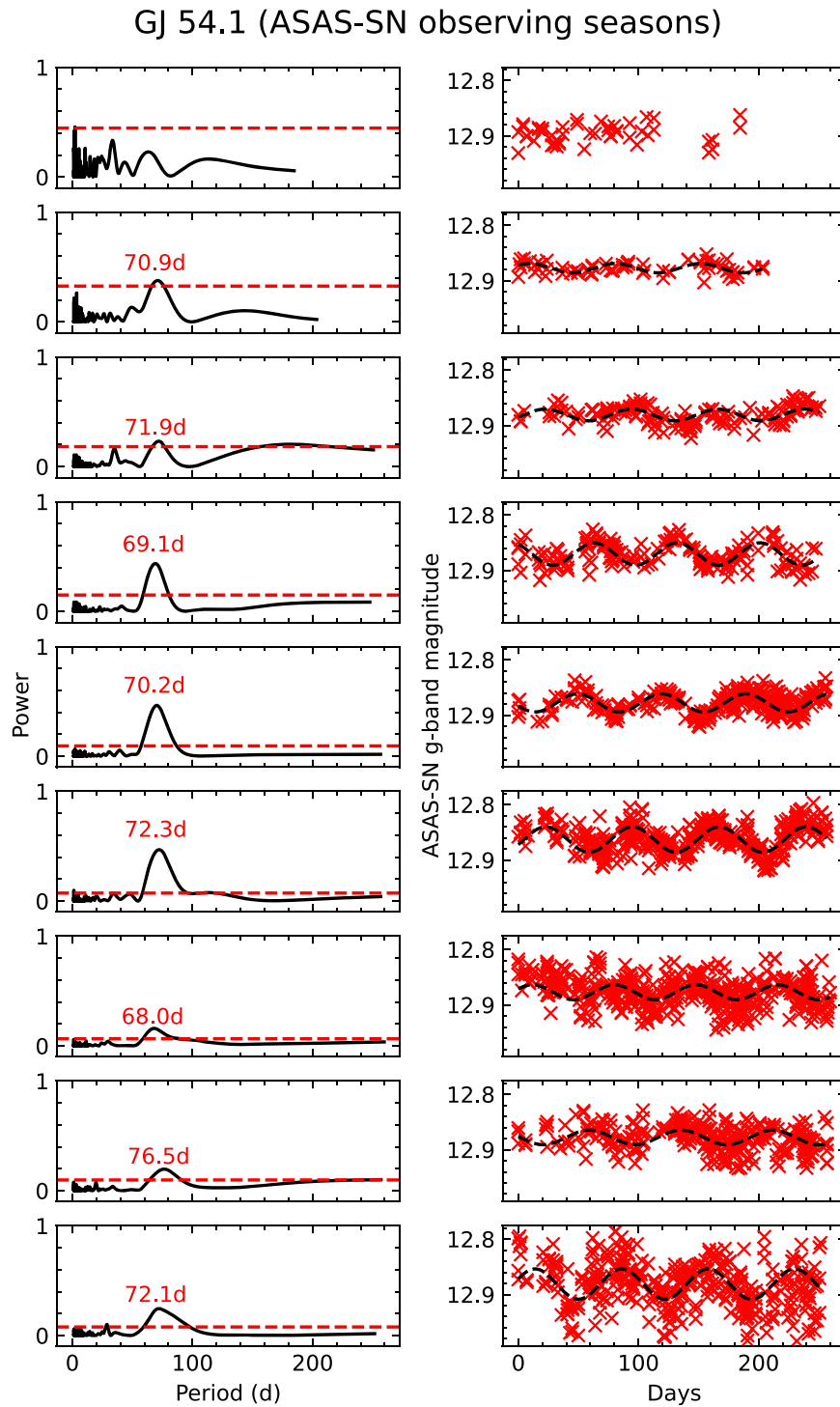
Figure 1. L–S periodograms (left) computed from ASAS-SN observing seasons (right) on GJ 54.1. Dashed red lines (left) show the power thresholds for FAPs of 0.1%. Dashed black lines (right) show optimized sine fits using the period of the tallest peak in the corresponding periodogram.
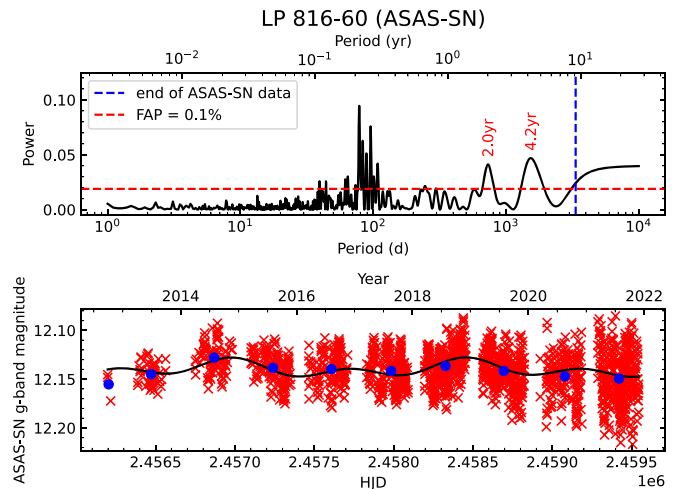
or only the best-fitting component was remaining. If the period (s) of the remaining component(s) was within the period of observation, then we deem this cycle to be "well defined" - and poorly constrained otherwise.

3. Results

Rotation and cycle periods are presented in Table 1. All results from this work have FAPs ⩽ 0.1%.

3.1. Rotation Periods

Using the analysis procedures described in Section 2.6.1, high-confidence rotation periods were determined for all but two of our stars. For one exception, GJ 729, P_{rot} is shorter than 15 days, but TESS data were not available for our work. We therefore used the same method as for stars with longer rotation periods, computing the mean and standard deviation of similar significant peaks in each ASAS-SN observing season's periodogram; these periodograms are shown in Figure 5. This
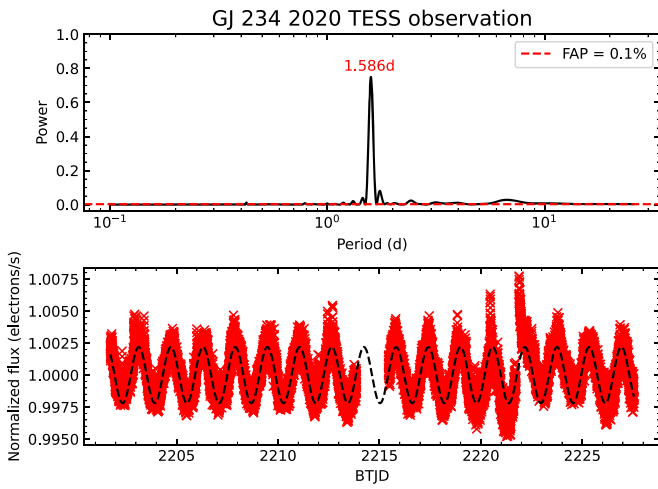
Figure 2. L–S periodogram (top) computed from the 2020 TESS observation of GJ 234 (bottom). The dashed red line (top) shows the power threshold for a FAP of 0.1%, and the dashed black line (bottom) shows the optimized sine fit using the period of the tallest peak in the periodogram.
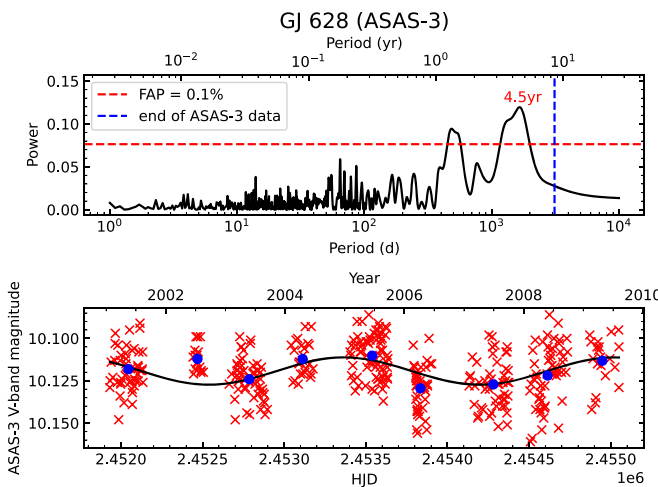

Figure 3. L–S periodogram (top) computed from ASAS-3 data on GJ 628 (bottom). The FAP = 0.1% power threshold is shown by the dashed red line, and the dashed blue line shows the time span of the data. The blue markers show the mean values (dates and magnitudes) for each observing season. The period of the labeled peak in the periodogram was used to create the sine fit in the bottom plot. The complete figure set (16 images) is available in the online journal (Figure Set 3).

(The complete figure set (16 images) is available.)

resulted in a rotation period of 2.9 ± 0.1 days, in agreement with Suárez Mascareño et al. (2016) and Ibañez Bustos et al. (2020), who found a rotation periods of 2.9 ± 0.1 days (from photometric monitoring) and 2.848 ± 0.001 days (from chromospheric indicators), respectively.

For the second exception, GJ 273, we could not determine a rotation period from our data sources. Breaking ASAS-SN data down by observing season, as described in Section 2.6.1, and shown in Figure 6, produced only one significant peak at ∼42 days. However, no other observing seasons showed any significant peaks at all. Computing periodograms from the entire ASAS-SN light curve, as shown in Figure 7, also produced no significant peaks with a period shorter than one year. Figures 6 and 7 show that this star has fewer ASAS-SN observations than many of the other stars in our sample, especially in the early seasons (which use *V*-band filters). The

Figure 4. Periodogram and ASAS-SN data for LP 816-60. The complete figure set (15 images) is available in the online journal (Figure Set 4).

(The complete figure set (15 images) is available.)

sparsity of these observations undoubtedly contributed to our inability to identify rotational modulations within this light curve. For these reasons, we adopted the P_{rot} of 115.9 ± 19.4 days measured by Suárez Mascareño et al. (2015) using HARPS Ca II H and K and Hα data.

Given analysis uncertainties and the inherent variation in rotational measurements caused by starspot evolution, migration in latitude and longitude, and differential rotation, our results are generally in good agreement with previous measurements. Where there are significant disagreements (GJ 234, GJ 628, and LP 816-60), we believe our measurements are more trustworthy given the higher quality and cadence of TESS and ASAS-SN data compared to the ASAS-3 data used by Suárez Mascareño et al. (2016). Note that two of our stars, GJ 317 and GJ 406, have P_{rot} values reported for the first time.

3.2. Cycle Periods

L–S analysis yields FAPs shorter than 0.1% using ASAS-3/-4 and/or ASAS-SN data for 12 stars, not including a few cases where the significant peak corresponds to a cycle period exceeding the period of observation. Below, we comment on three stars of particular note. For stars not mentioned below, light curves and associated L–S periodograms are provided in Figure Sets 1 (ASAS-3/-4) and 2 (ASAS-SN).

3.2.1. LP 816-60

Figure 4 provides strong evidence for at least one activity cycle in LP 816-60. From this figure, it is clear that there are two strong periodic signals in the LP 816-60 ASAS-SN light curve, with periods of 2.0 and 4.2 yr. Upon first inspection, one of these peaks could be interpreted as a harmonic of the other. Indeed, 4.2 is very close to double 2.0, and taking into account the uncertainties on these periods, one could well be a harmonic of the other.

Evidence presented by do J.-D. Nascimento et al. (2023, in preparation) suggests that it is not uncommon to measure cycles with P_{cyc} and $P_{cyc}/2$. In their paper, they interpret these results as the separate Hale (magnetic polarity) and Schwabe (activity, starspots) cycles having different amplitudes due to (for reasons that are currently unclear) one polarity being stronger. Given the two clear cycles visible in LP 816-60's ASAS-SN data, this star
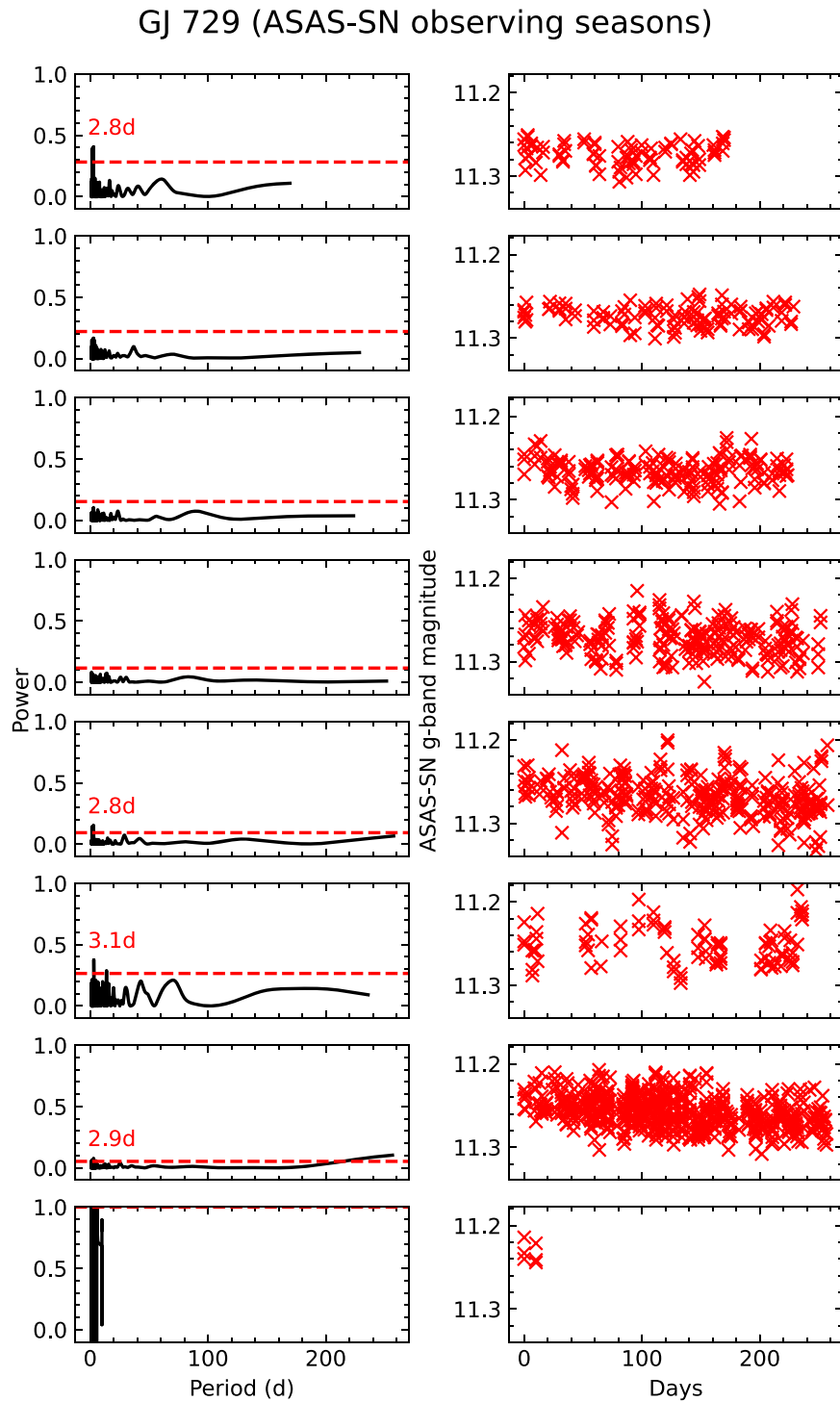
GJ 729 (ASAS-SN observing seasons)

Figure 5. L–S periodograms (left) computed from ASAS-SN observing seasons (right) on GJ 729. Due to the short inferred rotation periods, no sine fits are shown as the modulations would be unresolvable.

may therefore provide evidence that M dwarfs also possess (or, at least, appear to have) asymmetric polarity strengths. Another possibility is that both peaks are the result of a single quasiperiodic cycle, as discussed in Olspert et al. (2018a).

Alternatively, because these cycles have been inferred using optical photometry data, they could be the result of an observing effect. Assuming a 4.2 yr cycle period, it could be the case that for one-half of this cycle, starspots are preferentially generated out of our line of sight (i.e., $\sin(i) \ll 1$)—although the clear rotational modulations make this less likely. Without Zeeman-Doppler

imaging (ZDI; e.g., Hébrard et al. 2016) or X-ray observations (e.g., Wargelin et al. 2017), however, it is difficult to determine whether an observed cycle is the result of magnetic activity (specifically a Schwabe cycle) or some other phenomenon.

3.2.2. GJ 358

The GJ 358 ASAS-SN light curve (Figure 8) shows that the cyclic modulations appear to be reasonably well described by two sinusoidal functions, following the $P_{\rm cyc}$ and $P_{\rm cyc}/2$ rule
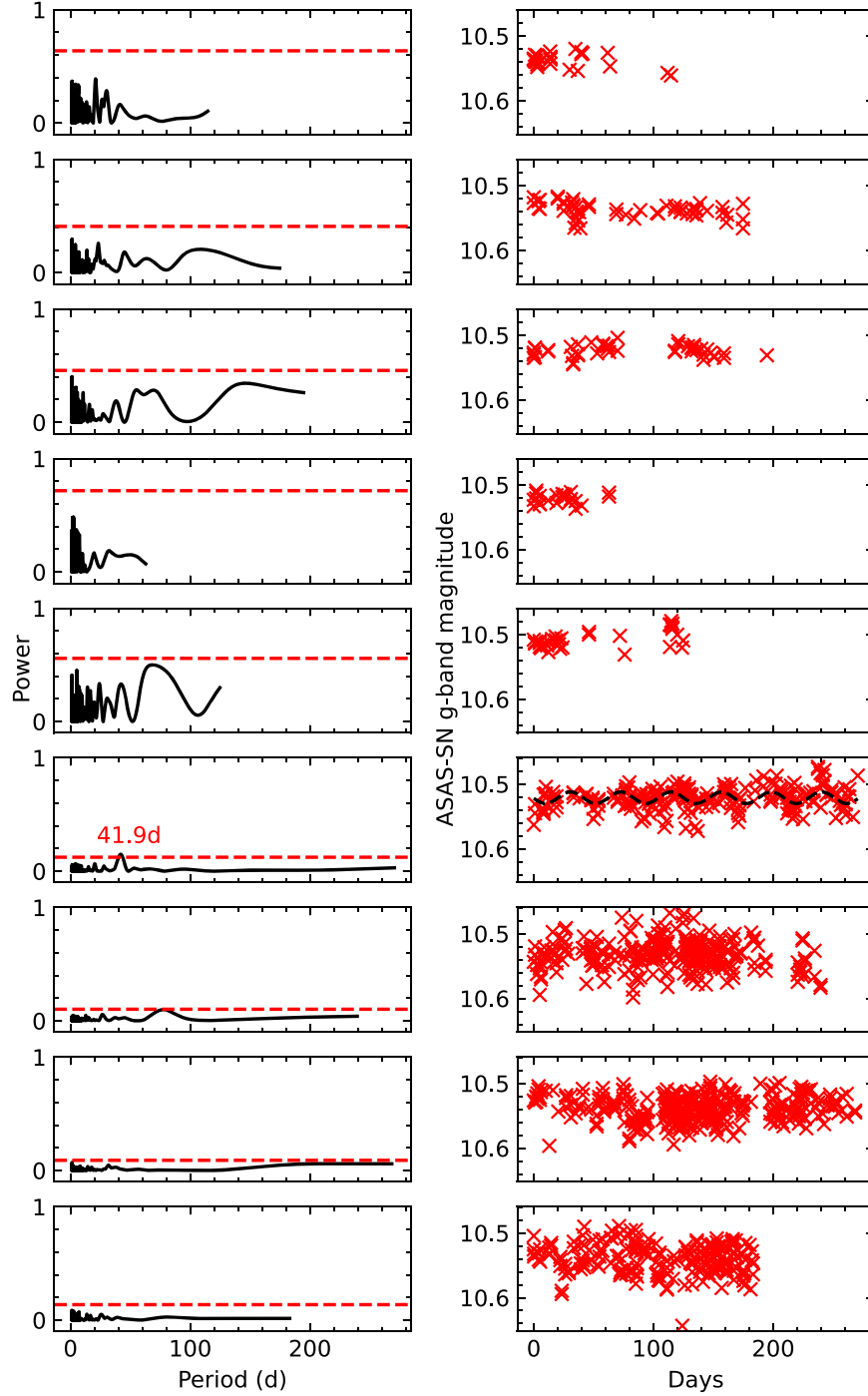
Figure 6. L–S periodograms (left) computed from ASAS-SN observing seasons (right) on GJ 273.

suggested by do J.-D. Nascimento et al. (2023, in preparation). Interestingly, both the ASAS-3 and ASAS-SN light curves (Figures 9 and 8) show long-term linear trends whose gradients are of opposite sign; this may suggest that GJ 358 exhibits a longer-term Gleissberg-esque cycle, although many more years of data will be needed to confirm this.

Further study of the light curves from ASAS-3 and ASAS-SN, both of which are shown in a single plot in Figure 10, reveals that the GJ 358 cycle period has been steadily

decreasing for at least the last 20 yr. ASAS-3 data show cyclic modulations with periods greater than four years, while the most recent modulation seen in ASAS-SN data has a period of just 1.5 yr. This star therefore appears to be quite unusual. Unfortunately, there is a ∼6 yr gap between ASAS-3 and ASAS-SN data on this object. This gap could be filled with ASAS-4 data, but these data are not publicly available. Analysis of these data would prove very interesting and might reveal, for example, whether the cycle period has changed
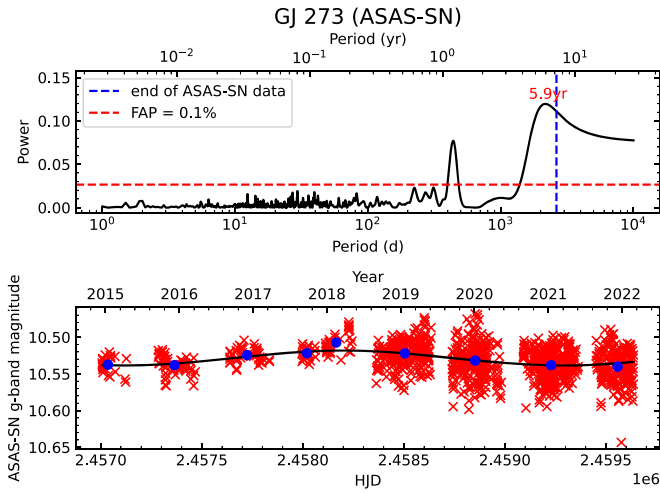
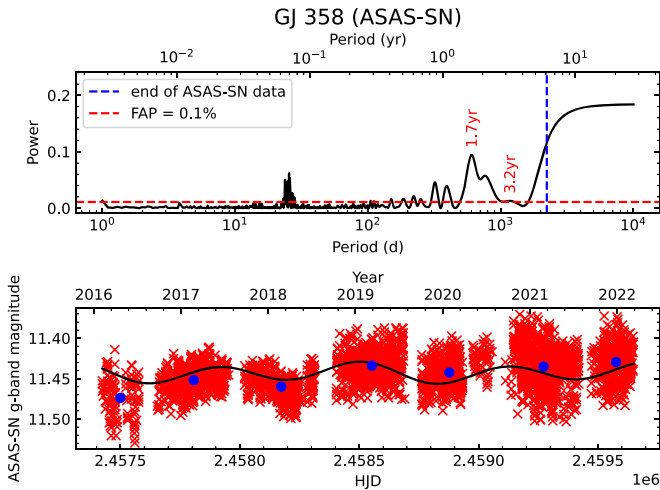**Figure 7.** Periodogram and ASAS-SN data for GJ 273.

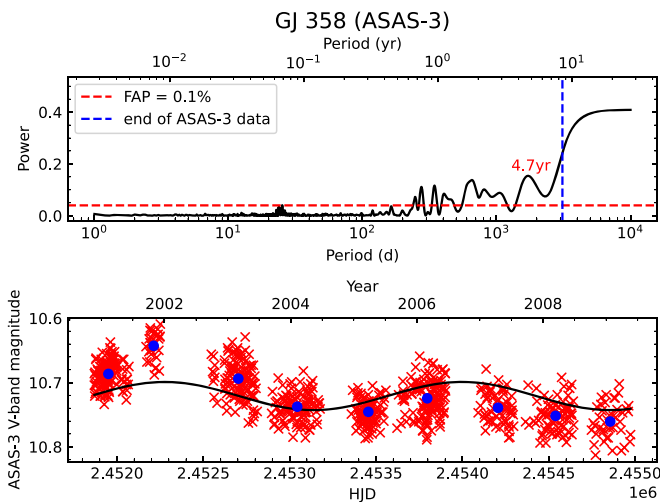**Figure 8.** Periodogram and ASAS-SN data for GJ 358.

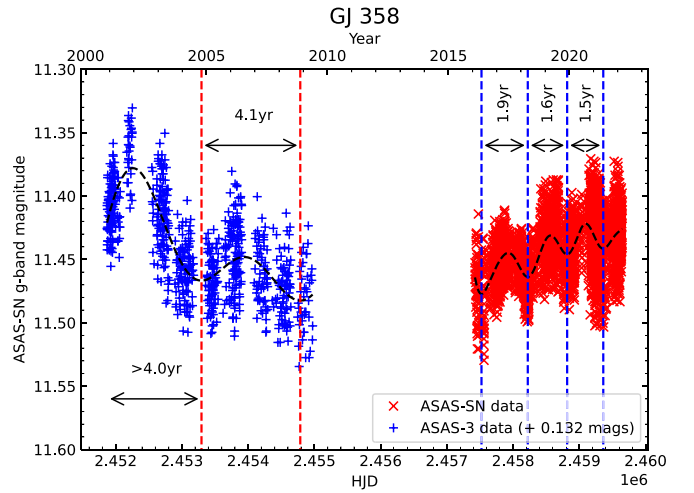**Figure 9.** Periodogram and ASAS-3 data for GJ 358.

Figure 10. GP fits (dashed black line) to ASAS-3 and ASAS-SN data (blue and red markers, respectively) on GJ 358. ASAS-3 data were color-corrected using Equation (1) and were then further offset to align them vertically with ASAS-SN data. Local minima in these GP fits are marked by vertical dashed lines, and the periods between successive minima are labeled.

period will reach a local minimum before increasing again. It is also unclear if this changing period is related to the long-term cycle suggested by the linear trends seen in the GJ 358 ASAS-3 and ASAS-SN data. Future observations of this object are therefore needed to better understand this seemingly exceptional cyclic activity.

3.2.3. GJ 551

GJ 551 (Proxima Centauri) is an interesting case for several reasons. It is the most well-studied example of a fully convective M star exhibiting cyclic activity, and it is the only fully convective star (in fact, the only M star) to have undergone long-term X-ray monitoring. Suárez Mascareño et al. (2016) found a 7 yr cycle in ASAS-3 data, and Wargelin et al. (2017) included an additional ∼5 yr of ASAS-4 data, plus UV and X-ray observations to further support this conclusion.

More recent optical monitoring data, however, are less clear, as reflected in the ASAS-SN results listed in Table 1 and shown in Figure 11, which includes ASAS-4 data extending into 2019 that were presented in Damasso et al. (2020). ASAS-3 and ASAS-4 data were cross calibrated (private communication, G. Pojmański), and then calibrated versus ASAS-SN data following the "overlapping data" procedures described in Section 2.2.1. As seen in Figure 11, periodic behavior is quite apparent at the beginning, but steadily weakens while average brightness increases. We suspect that the increasing stellar contamination noted in Section 2.3 is significantly affecting the data, but attempting to model and correct the contamination is beyond the scope of this paper. In contrast, X-ray data from Swift, now spanning more than 12 yr (with some gaps), indicate well-behaved cyclic behavior, currently with a period of ∼9 yr (B. J. Wargelin et al. 2023, in preparation).

3.3. Periodicities and Magnetic Cycles

It should be noted that some of the cycles presented in Table 1 may not be related to a star's global magnetic field, but could be the result of other physical phenomena (or, if they are, may not be Schwabe cycles; do J.-D. Nascimento et al. 2023, in preparation). For example, Rossby waves (horizontally flowing
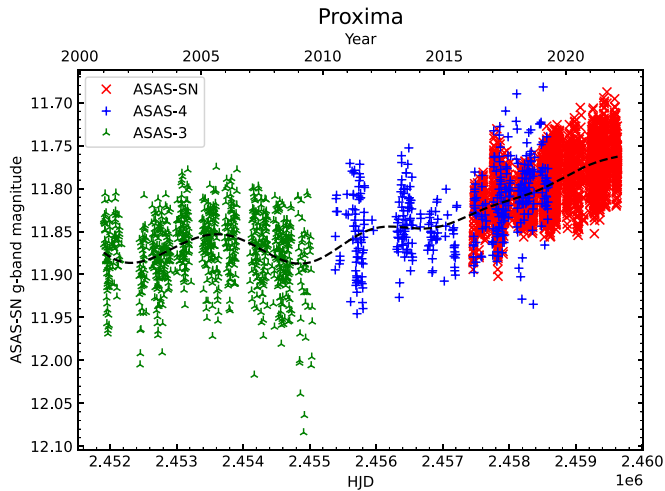
monotonically, and when and how the longer-term trends seen in ASAS-3 and ASAS-SN data intersected.

At present, it is also unclear whether GJ 358's cycle is approaching some kind of (quasi-)steady state, or if this cycle

Figure 11. GP fit (dashed black line) to the Proxima ASAS-3, ASAS-4, and ASAS-SN data.

eddies in the convective zone/photosphere), as seen in the Sun, can act as dynamos (e.g., Gilman 1969), leading to perceived cyclic activity that is not necessarily related to the star's global magnetic field.

In the case of our Sun, there is also the Rieger cycle (Rieger et al. 1984), where hard solar flares are observed to occur in groups with a mean spacing of ∼154 days. Similar cycles surely exist in other stars; while flares are a result of magnetic activity, they are local effects, and it is not well understood how they relate to a star's global magnetic field - even in the case of our Sun (e.g., Toriumi & Park 2022).

3.4. Phase Matching

One way to assess the validity of a star's apparent cycles is to see if they are consistent through ASAS-3 and ASAS-SN data. If the best-fitting cyclic models from both data sets show a reasonable level of agreement (in terms of both phase and amplitude) where they overlap, then these cycles are more likely to be real. Note, however, that this method assumes a roughly constant cycle period, which, as discussed in Section 1, may not always be the case.

To investigate the amplitude and phase matches, we extend the cycles identified in Table 1 such that the ASAS-3 and ASAS-SN cyclic models for each star overlap by one year. In addition to this, we also offset the ASAS-3 data such that the mean magnitude of this light curve is the same as the mean magnitude of the ASAS-SN light curve, thus allowing easy comparison of the models' phases and amplitudes. Example plots are shown in Figure 12, showing the results for GJ 273, GJ 234, and GJ 447. All phase-match plots (10 images) are provided in Figure Set 12. Note, however, that we place little emphasis on these plots; indeed, they are primarily included so that the inferred cycles from both data sets can be more easily compared.

As can be seen in the top panel of Figure 12, both the ASAS-3 and ASAS-SN cyclic models on GJ 273 agree very well, in terms of both phase and amplitude, where they overlap. We interpret this as enhanced evidence for these cycles being real. On the other hand, GJ 234 (middle panel of Figure 12) shows good amplitude agreement, but poorer phase agreement, while GJ 447 (bottom panel of Figure 12) shows poor agreement in both cases. In the final column of Table 1, we assign each star's ASAS-3 and ASAS-SN cycles a subjective phase-match grade
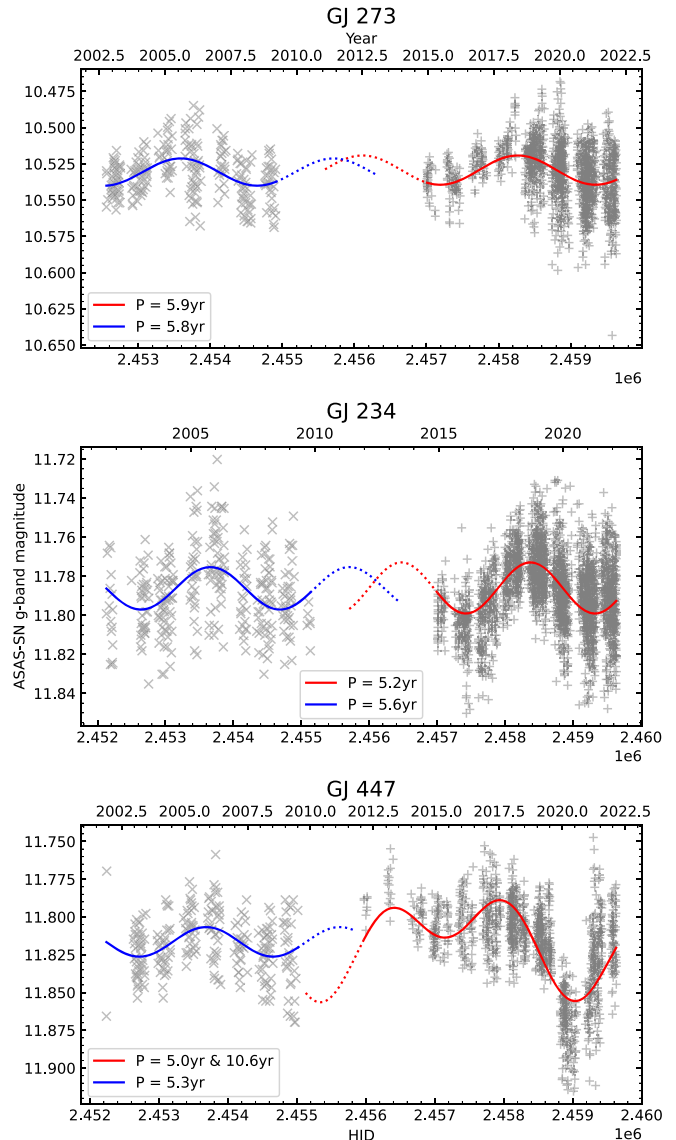

Figure 12. Plots of the cyclic models found from ASAS-3 (blue line) and ASAS-SN (red line) data for GJ 273, GJ 234, and GJ 447 from Table 1, showing good, fair, and poor agreement, respectively. The complete figure set (10 images) is available in the online journal (Figure Set 12).

(The complete figure set (10 images) is available.)

of either good, fair, or poor. For reference, we judge that GJ 273, GJ 234, GJ 447 show good, fair, and poor phase agreement, respectively. The remaining plots are provided in Figure Set 12.

4. Discussion

With rotation and cycle parameters in hand, we can investigate correlations among various physical quantities. First, however, we must determine a largely theoretical quantity for each star: its convective turnover time, τ.

4.1. Determining Convective Turnover Times and Rossby Numbers

The convective turnover time is a measure of how long it takes for convection to move material from the bottom of the

convective zone to the top, or vice versa, and it is related to the ratio of the thickness of the convective envelope (thin in F stars, fully convective by $\sim$M3.5) and the mean convective velocity (which increases with temperature). To compare stars with differently sized convective zones, temperatures, and rotation periods, a dimensionless quantity known as the Rossby number, Ro, is commonly used. Another dimensionless quantity is the linear $\alpha\Omega$ dynamo number, D, a measure of the dynamo's strength, which is proportional to Ro^{-2}. The Rossby number of a star is defined as

$$Ro = \frac{P_{\rm rot}}{\tau}, \qquad (3)$$

where $P_{\rm rot}$ is the rotation period, and τ is the convective turnover time. Note, however, that there are two definitions for the convective turnover time: a local and a global definition. The local convective turnover time, τ_L, applies to the bottom of the convective zone (in the tachocline, where the main dynamo amplification takes place in some models), while the global convective turnover time, τ_G, is an average over the entire convective zone. The global convective turnover time is therefore a better quantity for M stars, where the tachocline is negligible or absent.

The choice of a convective turnover time is important. We need both a local (for tachocline-based dynamos) and a global (for full convection zone dynamos) τ, which we denote τ_L and τ_G, respectively. Since we are interested in the operation of dynamos, a τ derived from any indirect activity diagnostic (e.g., Ca II HK or X-ray emission) is of dubious utility. This is because these empirical τs implicitly assume that the function $f(M, \log g, [\mathrm{Fe/H}])$ that best connects the given emission to rotation can be defined to be τ, ignoring the complex physics connecting magnetic flux to the heating that produces the emission in question (e.g., Cuntz et al. 1999). The hidden inclusion of this additional heating physics makes these empirical τs inappropriate for understanding how dynamos themselves operate. Note that a τ derived by best-fitting rotation with unsigned magnetic flux measurements would be more appropriate. This has not yet been attempted to our knowledge, likely because data on unsigned fluxes are sparse and generally come with large errors (e.g., Saar et al. 1994; Reiners 2012). Calculating such a τ is beyond the scope of the current work; however, new flux measurement methods may make it feasible in the near future (e.g., Lehmann et al. 2015; Mortier 2016).

Unfortunately, theoretically based τs are also problematic. Due to uncertainties concerning the M dwarf internal structure near the fully convective limit (Baraffe & Chabrier 2018; Jao et al. 2022), any purely theoretical τ is at best approximate at low masses (Jao et al. 2022). There are also problems defining a local τ in the center of fully convective stars. Indeed, with no convection zone bottom, the tachocline concept driving the need for a local τ requires modification itself. Fortunately, a recent paper has worked to improve τ models in low-mass stars (Landin et al. 2023). We adopt their values here at age $\approx$1Gyr. This is post-zero-age main sequence (ZAMS) for all masses here except 0.1 $M_\odot$, but we note from their Figure 1 that $\tau_G(0.1M_\odot)$ evolves negligibly for ages >0.3 Gyr. Indeed, over the mass range considered here, τ varies little along the main sequence, except at the highest masses, where differences of $\sim$30% may accrue at age extremes. We use the V–K_S versus $T_{\rm eff}$ relation of Pecaut & Mamajek (2013; and later improvements; Mamajek, E.E. 2021, private communication)
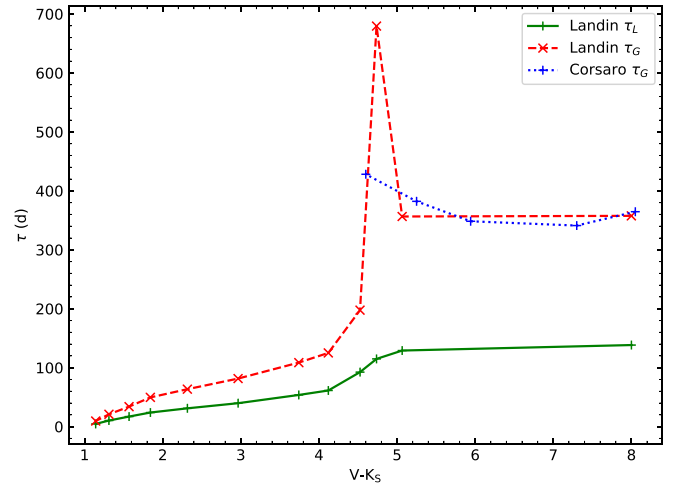

Figure 13. Convective turnover time (in days) vs. V–K_S color index from Landin et al. (2023). The dashed red line shows the global turnover time (τ_G), the solid green line shows the local turnover time (τ_L), and the dotted blue line shows the scaled version of an independent τ_G calculation for fully convective stars of Corsaro et al. (2021) that agrees well, except in the narrow zone 3250 K $\leqslant T_{\rm eff} \leqslant$ 3400 K. We adopt τ (Landin) everywhere except for τ_G for $T_{\rm eff} <$ 3400 K (V–$K_S \approx$ 4.6), where we transition to the scaled τ_G (Corsaro); see text for details. τ (Landin) have been truncated (using linear interpolation) at V–$K_S = 8$; see Table 1.

to match to our stars. As a cross check, we compare the calculations at low mass with a different kind of empirical τ calculation based purely on stellar properties - derived equating the star's output bolometric flux with convective flux (Corsaro et al. 2021). They find $\tau_G \propto R[M/(LR)]^{1/3} \propto M^{1/3}T_{\rm eff}^{-4/3}$ for fully convective stars, where M, L, and R are the stellar mass, luminosity, and radius, respectively (taken from Pecaut & Mamajek 2013). We find that a scaled version of these physics-based empirical τ_G for the most part compares well with the new τ_G of Landin et al. (2023; Figure 13; where we also display their τ_L). The exception is in the narrow temperature range 3250 K $< T_{\rm eff} <$ 3400 K, very near the fully convective boundary, where τ_G (Landin) shows a spike that τ_G (Corsaro) does not. (We also note that $T_{\rm eff}(0.1M_\odot)$ is cooler in Landin et al. 2023). We suggest that τ_G calculations near the stellar center may still have problems (Jao et al. 2022), and in keeping with the idea that τ_L and τ_G should roughly scale with each other (e.g., Montesinos et al. 2001), we adopt the Corsaro values for $T_{\rm eff} \leqslant$ 3400 K. We use τ_G for fully convective stars, and either τ_G or τ_L otherwise, depending on the circumstances.

With estimated convective turnover times and Rossby numbers for our 15 M-type stars, we then used results from Saar & Brandenburg (1999), Lehtinen et al. (2016), and Olspert et al. (2018a) to gather a comparison sample of 40 F-, G-, and K-type stars with robust, well-defined cycles. Of these 40 stars, listed in Table 2, 10 have double cycles. Note, however, Olspert et al. (2018a) used multiple different methods to identify stellar cycles; for consistency with our approach, we use results obtained via their harmonic model (see Section 2.5 for more details). To estimate the convective turnover times of these stars, we use the method described above.[10] We note, however, that we exclude HD 18256 (F6) as it is too hot for our τ estimations; interestingly, in their study of Ca II H and K cycles in 15 stars, Baliunas et al. (2004) found that this star had

---

[10] Note: while we do not include a plot of τ_L versus B–V, the stars from Table 2 correspond to roughly the range $1 \leqslant V$–$K_S \leqslant 3.5$ in Figure 13.

Table 2
Activity Cycles for FGK Type Stars Taken from Previous Works

Star	Spectral Type	$B - V$	$P_{\rm rot}$ (d)	$P_{\rm cyc}$ (yr)	References	Star	Spectral Type	$B - V$	$P_{\rm rot}$ (d)	$P_{\rm cyc}$ (yr)	References
HD 1835	G2.5	0.66	7.78	9.1	1	HD 18256	F6	0.45	3	6.8	1
HD 20630	G5	0.68	9.24	5.6	1	HD 76151	G2	0.67	15	2.52	1
…	…	…	…	…	…	…	…	…	14.4	15.9	3
…	…	…	…	…	…	…	…	…	…	5.09[a]	3
HD 82443	G9	0.77	5.38	3.89	1	HD 115404	K2	0.94	18.47	12.4	1
…	…	…	…	20	2	…	…	…	…	…	…
HD 149661	K1	0.84	21.07	16.2	1	HD 165341	K0	0.86	19.9	15.5	1
…	…	…	…	4	…	…	…	…	…	5.1	…
HD 100180	F9.5	0.57	14	3.6	1	HD 190406	G0	0.61	13.94	2.6	1
…	…	…	…	…	…	…	…	…	…	16.9	…
HD 1405	K2	0.95	1.756	8	2	HD 70573	G1/2	0.62	3.314	6.9	2
HD 82558	K1	0.93	1.604	14.5	2	HD 116956	G9	0.80	7.86	14.7	2
…	…	…	…	18	…	…	…	…	…	…	…
HD 135599	K0	0.83	5.529	14.6	2	HD 171488	G2	0.62	1.345	9.5	2
Sun	G2	0.631	26.09	10.89	3	HD 103095	K1	0.75	34.3	7.13	3
HD 10476	K1	0.84	35.6	10.6	3	HD 10780	K0	0.81	22.14	7.53	3
HD 114710	F9.5	0.59	11.99	16.56	3	HD 146233	G2	0.65	22.62	11.2	3
HD 152391	G8.5	0.76	10.62	9.03	3	HD 155886	K2	0.85	20.58	10.44	3
…	…	…	…	13.73	…	…	…	…	…	5.0	…
HD 156026	K5	1.16	16.69	17.89	3	HD 160346	K3	0.971	32.0	7.21	3
HD 16160	K3	0.98	48.58	12.45	3	HD 165341A	K0	0.86	19.33	5.19	3
HD 166620	K2	0.87	42.1	16.16	3	HD 185144	K0	0.87	27.7	6.66	3
HD 201091	K5	1.18	35.54	7.16	3	HD 201092	K7	1.37	34.55	11.65	3
…	…	…	…	21.09	…	…	…	…	…	…	…
HD 219834B	K2	0.91	34.78	9.32	3	HD 26965	K0	0.82	38.65	10.66	3
HD 32147	K3	1.06	33.7	11.13	3	HD 3651	K0.5	0.83	37.0	16.98	3
HD 37394	K1	0.84	11.49	5.83	3	HD 4628	K2.5	0.90	37.14	8.56	3
…	…	…	…	…	…	…	…	…	…	5.79	…
HD 78366	G0	0.60	9.519	14.63	3	HD 81809	G1.5	0.80	41.66	8.11	3

Notes.
[a] Excluded from plots (see Section 4.1.1).
References. (1) Saar & Brandenburg (1999), (2) Lehtinen et al. (2016), (3) Olspert et al. (2018a).

by the far the largest anharmonicity, which is a measure of the deviation from single-period sinusoidal behavior, in their sample.

4.1.1. Data Selection

When gathering our sample of FGK stars from other works, we only included cycles in known (or likely) dwarfs. When the results of Saar & Brandenburg (1999) are compared with those of Olspert et al. (2018a), there are 17 stars in common. Since Olspert et al. (2018a) had longer time series for their analysis, we favor their results in most cases. We note an exception below, however.

Saar & Brandenburg (1999) found a single 2.52 yr cycle in HD 76151, while Olspert et al. (2018a) found 5.0 yr and 15.9 yr cycles using their harmonic model. We interpret this 5.0 yr cycle as a Hale cycle (born of a polarity asymmetry in the HD 76151 magnetic field; do J.-D. Nascimento et al. 2023, in preparation). For this reason, we reject this 5.0 yr cycle. We also note that this 5.0 yr cycle resides between the I and A branches when it is plotted in $P_{\rm cyc}/P_{\rm rot}$–Ro^{-1} space, which we interpret as stronger evidence that this is not a Schwabe cycle (see Section 4.7).

4.2. $A_{\rm cyc}$ versus $P_{\rm cyc}$

Figure 14 shows a plot of cycle amplitude against period for the well-defined cycles in Table 1, along with a least-squares fit

following $A_{\rm cyc} \propto P_{\rm cyc}^{0.94\pm0.11}$. When fitting this power law, only stars with a single well-defined cycle per data set were used (i.e., when a star had a single cycle in both ASAS-3 and ASAS-SN data, then both cycles were used). The suspect 5.1 yr ASAS-4 cycle of Proxima was ignored during the fitting (see Section 2.3).

As can be seen in Figure 14, cycles with longer periods generally also have larger amplitudes (ignoring stars with more than one concurrent cycle, whose cycles are connected with dotted lines and that are shown with faded markers). We speculate that this may be because longer periods allow a greter buildup of magnetic energy, resulting in a more pronounced cycle; this process is interrupted in stars with more than one concurrent cycle, and therefore they appear to contradict this trend. This relation may also explain why short-period cycles are detected less frequently in ASAS-3 data, which are noisier than their ASAS-SN successor. It may be the case that short-period cycles are present in ASAS-3 data, but cannot easily be resolved as their amplitudes are comparable to the ASAS-3 noise level.

Since stars with more than one well-defined cycle per data set were excluded from the power-law fit shown in Figure 14, it is interesting to note where these excluded cycles reside in relation to this fit. Indeed, it can be seen that for stars with two concurrent cycles, one circle is usually closer to this power law than the other; these other cycles may therefore be "false cycles" (Section 3.3) or indications of a multibranched relation,
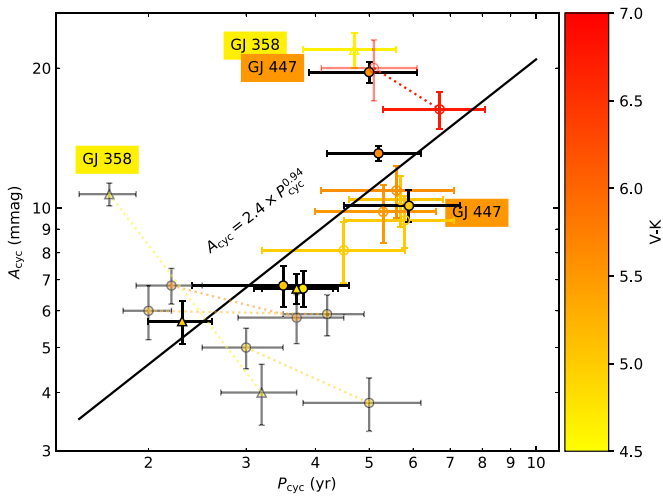
Figure 14. Cycle amplitude (in millimagnitudes) against cycle period (in years) using the well-defined cycles from Table 1. Color-only markers show cycles inferred from ASAS data, markers with dark outlines are from ASAS-SN data, fully convective stars use circle markers, partially convective stars use triangle markers, faded markers denote that these points were ignored during fitting, and concurrent cycles within the same star are connected with dotted lines. The outlier points for GJ 358 and GJ 447 (with colored labels) are discussed in the text.

Figure 15. Plot of the cycle period (in years) against the Rossby number, including FGK type stars from Table 2. For the M dwarfs analyzed in this work, filled markers represent cycles inferred from ASAS-SN data, empty markers are from ASAS-3/-4 data, fully convective M stars use circles, and partially convective M stars use triangles. Multiple cycles within the same star (and, for our M dwarfs, found within the same data set) are connected by dotted lines.

as seen by some in the P_{cyc}–P_{rot} relation (e.g., Saar & Brandenburg 1999; Böhm-Vitense 2007; Lehtinen et al. 2016). It should also be noted that A_{cyc} can be quite variable (more so in the Sun than in P_{cyc}), and so some outliers may be expected. That said, the (somewhat tentative) agreement among these excluded cycles is interesting, and we interpret this as further evidence for this relation between cycle amplitude and period.

Multiple branches in the A_{cyc}–P_{cyc} relation may explain why, for example, the ASAS-3 cycle of GJ 358 and ASAS-SN cycle of GJ 447 are outliers from the power law shown in Figure 14. As discussed in Section 3.2.2, however, GJ 358 already appears to be a highly unusual star. GJ 447, on the other hand, does have a second cycle period in Table 1, although it is not well constrained. This second cycle has an estimated period of 10.6 ± 6.9 yr and an estimated amplitude of 21.5 ± 1.0 mmag, which would put it very close to the power law shown in Figure 14, although with a large period uncertainty.

Using chromospheric Ca II H and K data on FGK stars, Saar & Brandenburg (2002) found stronger evidence for multiple branches in the A_{cyc}–P_{cyc} relation owing to their larger sample of stars. However, as the amplitudes from Saar & Brandenburg (2002) are from chromospheric indicators, they are not directly comparable to our photometric amplitudes. It would be very interesting to see how the photometric cycle amplitudes of F–M type stars compare, but this is left to future work.

In the case of our Sun, the solar cycle does not have a strict 11 yr periodicity; indeed, the ~4 year range of the solar P_{cyc} (Donahue & Baliunas 1992) is fully $\pm 18\%$ of the average value. Moreover, if a given solar cycle has a shorter than average period, then it will usually have a larger than average amplitude, and vice versa (related to the Waldmeier effect; Waldmeier 1935). For the M-type stars analyzed in this work, the observation intervals cover only a handful of cycles in the best case, so it is difficult to determine whether these cycles reflect a natural range in P_{cyc} as seen in the Sun. However, from Figure 14, it is clear that for M-type stars that exhibit two apparent cycles, the shorter cycle usually has a greater
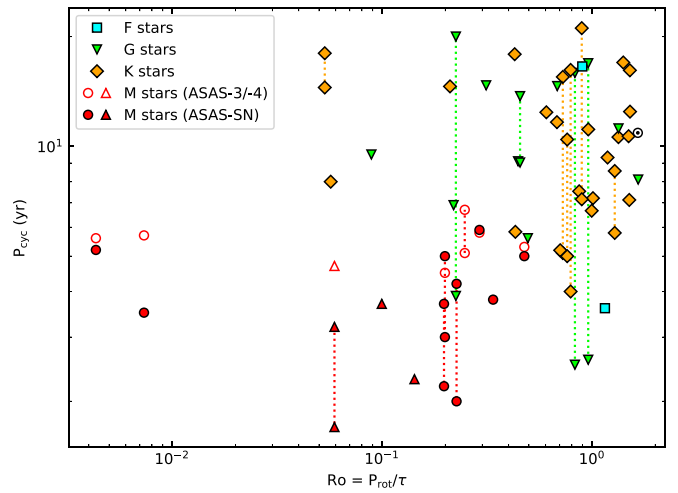
amplitude; in cases where the shorter P_{cyc} is approximately half the longer P_{cyc}, this is consistent with one polarity being stronger than the other (i.e., a Hale, rather than a Schawbe, cycle, as suggested by do J.-D. Nascimento et al. 2023, in preparation). Alternatively, if, as Olspert et al. (2018a) suggest, these double cycles are the result of a single quasiperiodic cycle, then perhaps this suggests that M dwarfs behave similarly to the Sun - with shorter than average cycles having greater than average amplitudes, and vice versa.

4.3. P_{cyc} versus P_{rot} and Ro

The plot of the cycle period against rotation period for the well-defined cycles in Table 1, along with previously detected cycles in FGK stars presented in Table 2, shows high scatter, without strong correlations. However, convective zones are believed to be a key ingredient of stellar cycles, and these are not accounted for in this plot. We therefore place little emphasis on this plot (and choose to not include it here) as it ignores a major physical parameter of current stellar cycle models: the Rossby number.

Figure 15 plots the cycle period against the Rossby number for the well-defined cycles presented in Table 1, along with the previously detected cycles in FGK stars presented in Table 2. This figure shows that when the convective turnover time is accounted for in the form of the Rossby number, M-type stars appear to have similar cycles to those of FGK stars at equivalent Ro. However, it is clear that our M dwarfs favor shorter cycle periods, extending the lower cluster of FGK stars to lower P_{cyc}. M dwarfs also isolate themselves at low Rossby numbers, although this may be a sampling effect; perhaps M dwarfs extend the upper cluster of FGK stars to lower Ro as well.

In Figure 15, the longer cycle periods seen in FGK stars likely reflect the fact that these stars have generally been monitored over longer periods than M dwarfs. The evidence that M dwarfs exhibit shorter P_{cyc} (relative to FGK stars) is strong, but we also found indications of longer, currently unresolvable or poorly constrained cycles in 11 of our M
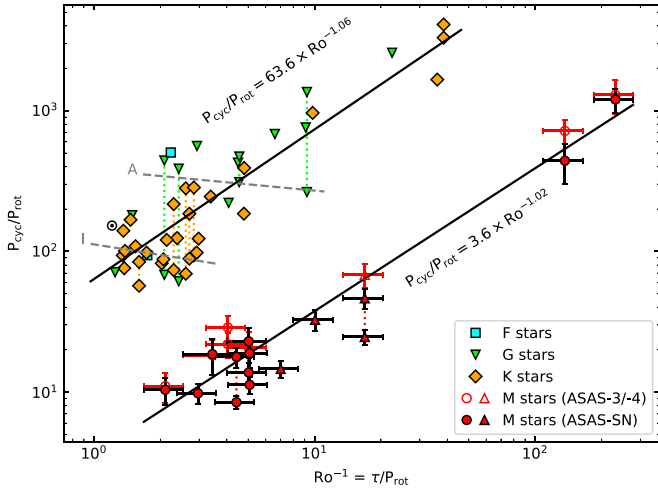
Figure 16. Plot of $P_{\rm cyc}/P_{\rm rot}$ against the inverse Rossby number, including FGK type stars from Table 2. The dashed gray fits show the A and I branches from Saar & Brandenburg (1999; which have been refit using our updated sample), while the black power-law fits were found in this work. The global convective turnover time was used to compute Ro for all cycles in this figure. For the FGK stars, because some of our sample did not include uncertainties on their cycle/rotation periods, we weighted all FGK cycles equally; for our M dwarfs, we assumed a $\pm 20\%$ uncertainty on τ.

dwarfs. Reproducing these figures with another 10 yr of ASAS-SN data may therefore prove interesting.

4.4. $P_{\rm cyc}/P_{\rm rot}$ versus Ro^{-1}

Figure 16 shows a plot of the cycle period divided by the rotation period against inverse Rossby number for the well-defined cycles presented in Table 1, along with the previously detected cycles in FGK stars presented in Table 2.

The power-law fit to the M-dwarf data in Figure 16 shows that these data follow the relation

$$\frac{P_{\rm cyc}}{P_{\rm rot}} = (3.6 \pm 1.2) \times Ro^{-1.02 \pm 0.06}. \tag{4}$$

Similarly, Figure 16 shows that FGK stars follow the relation

$$\frac{P_{\rm cyc}}{P_{\rm rot}} = (63.6 \pm 1.1) \times Ro^{-1.06 \pm 0.09}, \tag{5}$$

suggesting that $P_{\rm cyc} \propto \tau$ for all stars, in contrast to the results of Saar & Brandenburg (1999)—shown by the A and I branches (which we have refit using our updated sample).

Brandenburg et al. (1998) and Saar & Brandenburg (1999) interpreted the ratio of $P_{\rm cyc}/P_{\rm rot}$ as a measure of the α effect, based on the simple $\alpha\Omega$ dynamo model proposed by Robinson & Durney (1982) and Noyes et al. (1984). In this framework, Equations (4) and (5) suggest that M dwarfs have weaker α effects than FGK type stars at equivalent Rossby numbers (note that the scaling constant in Equation (4) is 17.7 times smaller than in Equation (5)). This result could be explained by considering the physical properties of these stars. Since M-type stars have deeper convective zones and consequently longer turnover times, longer rotation periods are needed to obtain similar Rossby numbers. Longer rotation periods therefore mean that the Coriolis forces that act within these convective zones are weaker, resulting in less helical turbulent convection. Furthermore, the average convective velocities themselves are

lower in these cooler stars; both these properties act to reduce the α effect.

Note, however, that the above explanation would suggest a smooth transition from F to M in Figure 16. In contrast, this figure shows a gap between FGK and M stars. Perhaps, because M stars are (almost) fully convective and therefore have (almost) no tachocline, this causes a significant change in the α effect. Alternatively, this gap could simply be the result of our limited sample of stars, which includes two K5s stars and one K7 star, but then no stars until M3. Clearly, Figure 16 needs to be extended to cover a wider range of stars, with a wide range of physical properties and rotation rates, to better understand whether this gap is real - and if so, what may be causing it.

4.5. α and Ω Effect Scaling

The axes of Figure 16 have the benefit of being dimensionless, and Ro in particular is directly related to the mean-field dynamo number, D, as mentioned in Section 4.1. Clusters and trends within the data can thus provide insights into the underlying dynamo properties. Indeed, we have already discussed the implications of the scaling constants of Equations (4) and (5); below, we discuss the implications of the power-law indices of these equations.

According to most theoretical models (e.g., Ruediger & Kichatinov 1993), the α effect should be quenched with growing magnetic fields, based on the reasoning that the stronger a star's magnetic field, the stronger the suppression of cyclonic convection (i.e., the α effect). This paradigm persisted until Saar & Brandenburg (1999) found evidence suggesting that the α effect may be antiquenched on their A and I branches. Here, with the benefit of a more focused sample of stars (no binary or evolved stars), we reinvestigate these claims.

Using a 2D nonlinear dynamo model, Tobias (1998) found

$$P_{\rm cyc} \propto D^{\gamma}, \tag{6}$$

where D is the dynamo number, and $-0.67 \leqslant \gamma \leqslant -0.38$. To explore the role of quenching in a simpler linear 1D dynamo model, Saar & Brandenburg (1999) defined a quenching index, q, such that

$$D \propto \alpha\Omega' \propto Ro^{-q-2}, \tag{7}$$

where Ω' is the radial DR, and

$$q = q_{\alpha} + q_{\Omega} - 2, \tag{8}$$

where q_{α} is the quenching index of the α effect (i.e., $\alpha \propto \Omega^{q_{\alpha}}$, with $\Omega \equiv \frac{2\pi}{P_{\rm rot}}$), and q_{Ω} is the quenching index of the Ω effect (i.e., $\Omega' \propto \Omega^{q_{\Omega}}$). From the solution of the standard dynamo equations (assuming a fixed wavenumber, k), Brandenburg et al. (1998) noted that the cycle frequency was given by

$$\omega_{\rm cyc} \equiv \frac{2\pi}{P_{\rm cyc}} \propto \left(\frac{\alpha\Omega' k L}{2} \right)^{\frac{1}{2}}, \tag{9}$$

where L is the dynamo length scale. Combining Equations (7) and (9), we have

$$P_{\rm cyc} \propto (\alpha\Omega')^{-\frac{1}{2}} \propto Ro^{\frac{q}{2}+1}, \tag{10}$$

or

$$\frac{P_{\rm cyc}}{P_{\rm rot}} \propto Ro^{\frac{q}{2}}. \tag{11}$$

Since Figure 16 suggests that the relation between $P_{\rm cyc}/P_{\rm rot}$-Ro can be described by a power law, where the power-law index can take various values, we can thus write

$$Ro^{\frac{q}{2}} \propto Ro^{\delta}, \tag{12}$$

where δ is the power-law index (i.e., $\delta = -1.04$ from Equation (4)). Thus we find (by combining Equations (8) and (12))

$$q_{\alpha} = 2\delta - q_{\Omega} + 2. \tag{13}$$

With this equation, we can infer the scaling of the α effect using the power laws plotted in Figure 16. First, however, we must estimate q_{Ω} (the quenching index for radial DR).

DR measurements are difficult and fraught with misidentifications (Aigrain et al. 2015; Basri 2018), but because good evidence suggests that surface DR scales linearly with rotation period for slower rotators (e.g., Saar 2011), it is reasonable to assume $q_{\Omega} \approx 1$; for saturated activity stars (discussed in Section 4.7), the dependence reverses, and $q_{\Omega} \approx -1.7$ (Saar 2011). We note that we are implicitly assuming that radial DR scales linearly with the measured surface DR.[11] With this assumption and using these q_{Ω}, we thus have

$$q_{\alpha} = 2\delta + 1, \tag{14}$$

in the unsaturated regime, and

$$q_{\alpha} = 2\delta + 3.7, \tag{15}$$

in the saturated regime. Using the power-law indices from Equations (4) and (5), we find $q_{\alpha,M} = -1.03$ and $q_{\alpha,\rm FGK} = -1.13$ in the unsaturated regime, and $q_{\alpha,M} = 1.67$ and $q_{\alpha,\rm FGK} = 1.57$ in the saturated regime. This suggests that the α effect is quenched with faster rotation in the unsaturated regime (but antiquenched in the saturated regime) similarly for FKG and M stars.

As mentioned previously, quenching of the α effect (in the unsaturated regime) is an expected result. In contrast, the α effect antiquenching that we find in the saturated regime is surprising - although antiquenching is supported by some magnetohydrodynamic (MHD) simulations (e.g., Chatterjee et al. 2011). We note that our findings in the unsaturated regime disagree with the results of Saar & Brandenburg (1999), whose limited sample of stars (and different assumptions about Ω effect scaling) led to the opposite conclusion for their A and I branches (note that the fit in Figure 16 is more consistent with their tentative transitional branch for faster rotators; see Lehtinen et al. 2016). That said, it should be noted that these results are based on a very simple dynamo model (Brandenburg et al. 1998), along with some debated assumptions about DR and α and Ω effect quenching (e.g., Barnes et al. 2005; Saar 2011).

4.6. Refining Our Selection of Convective Turnover Times

The clustering of stars at the end of the FGK sequence in Figure 16 (particularly around the putative I branch), together with the spread of the sequence in Ro, suggests that perhaps the concept of A and I branches is not completely without merit. If we consider possible A and I branches, however, we must note that we have not been self-consistent in our use of τ. If the I

---

11 Note, also, that some observers (e.g., Barnes et al. 2005) argued that DR has little or no dependence on rotation period, so our assumed q_{Ω} may be incorrect.
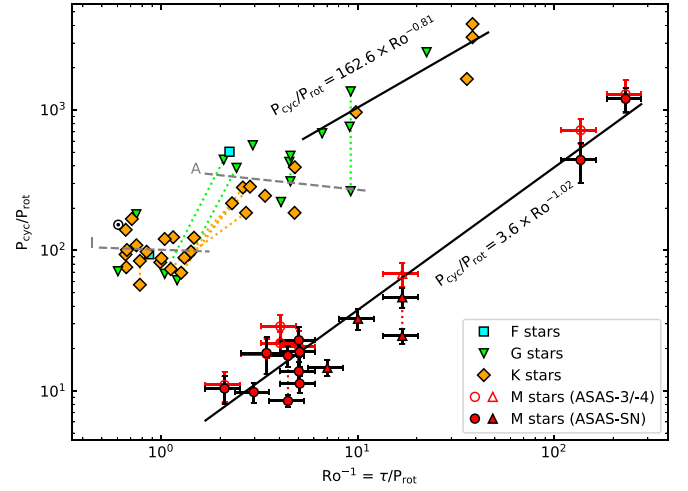

Figure 17. Similar to Figure 16, but with convective turnover times for cycles on the I branch calculated at the base of the convective envelope (i.e., using τ_L instead of τ_G). The A and I branches were also ignored when fitting a power law to the FGK stars.

branch is dominated by a tachocline dynamo (as assumed for the Sun), a local τ, τ_L, specifically computed for that location, is more suitable. Further, a fit to all the FGK stars together becomes inappropriate; the faster rotators (using τ_G, as before) and the slower I branch stars (using τ_L) should be treated separately. Using this distinction, we present the results in Figure 17.

Due to reasons that will become clear in Section 4.7, for stars with cycles on both the A and I branches, we deem the I branch cycle to be the primary and the A branch cycle the secondary. In a preliminary version of Figure 17, secondary cycles were plotted also using τ_L, but we noted that this caused larger scatter in the A branch fit ($\sigma = 1.07$ in log space). If we use τ_G for these secondary cycles, effectively assuming they arise from a convection zone dynamo still in operation, the A branch scatter is reduced by ∼20% ($\sigma = 0.81$; Figure 17). These new values modify Equation (5) to

$$\frac{P_{\rm cyc}}{P_{\rm rot}} = (162.6 \pm 0.2) \times Ro^{-0.81 \pm 0.17}, \tag{16}$$

but do little to change the spirit of the discussion in Section 4.5. A list of different model parameters, their goodness-of-fit metrics, and their implied q_{α} values is provided in Table 3.

4.6.1. GJ 358

If, as we propose in Section 4.6, F–K stars can have convective zone and tachocline dynamos operating simultaneously, then, for consistency, we should also consider this possibility for our partially convective M stars; we note, once again, the exceptional cyclic behavior of GJ 358. GJ 358 is one of (likely) four partially convective M stars in our sample, and is the only such star to show strong evidence for multiple concurrent cycles. Giving this star the same treatment as the F–K stars from the previous section, we might conclude that these cycles are from different dynamos. However, from a sample size of one, the division between the A and I branches for M stars is somewhat unclear.

When we assume that the GJ 358 cyclic behavior is the result of separate tachocline and convective zone dynamos, then its changing (notably, decreasing) cycle period makes some sense.

Since these two dynamos are (in our simple scenario) independent, then the cyclic behavior that we see is actually a superposition of two independent cycles; if these cycles have different (quasi)periods,[12] then observing a "cycle with a changing period" is not totally surprising.

Using the I branch and M dwarf fits from Figure 17, we can infer theoretical cycle periods for the GJ 358 tachocline and convective zone dynamos. Starting with the tachocline dynamo (i.e., the I branch), we find $P_{cyc} = P_{rot} \times 101.1 \times Ro^{0.05}$, which, when plugging in the values (using τ_L to compute Ro), gives $P_{cyc} = 6.5$ yr. This is 2σ above the 4.7 ± 0.9 yr period we infer from the GJ 358 ASAS-3 data, which is the longest period we were able to constrain for this star, and shifts it left in Figure 17 to $Ro^{-1} \approx 4$ (extending the I branch to larger Ro^{-1}). Now considering the convective zone dynamo, using the fit to all M stars, we find $P_{cyc} = P_{rot} \times 3.6 \times Ro^{-1.02}$, which gives $P_{cyc} = 4.4$ yr. This is consistent with the aforementioned ASAS-3 cycle period, and with the same Ro as shown in Figure 17. Perhaps these two dynamos are not totally independent, and interactions between the two cause more significant deviations from true periodic behavior than is typically observed in other stars, resulting in the decreasing cycle period we observe in Figure 10.

4.7. A New Interpretation of Dynamo Evolution

Indeed, our results here and those of Saar & Brandenburg (1999) may not necessarily be at odds; perhaps we are seeing a switch in dominance between two different types of dynamos with different properties. We largely set aside the discussion of the A branch here because more recent work casts doubt on its robustness/reality (e.g., Boro Saikia et al. 2018). We also skip discussion of the superactive (S) branch, which is occupied almost solely by binaries in which tidal rotational locking may alter the dynamo fundamentally and place it beyond the scope of the presumed single-star dynamos considered here.

We propose the following scenario. The most rapid rotators seem to have nearly solid-body rotation, for example, GJ 1243 (M4, $P_{rot} = 0.59$ d, $k/k_\odot = (\Delta\Omega/\Omega)/(\Delta\Omega_\odot/\Omega_\odot) \approx 0.01$; Davenport et al. 2020), LQ Hya (K2, $P_{rot} = 1.597$ days, $k/k_\odot = 0.028$; Kovári et al. 2004), or V889 Her (G2, $P_{rot} = 1.337$ d, $k/k_\odot = 0.045$; Kővári et al. 2011). With so little DR, their dynamos are likely a turbulent α^2 type or at best $\alpha^2\Omega$, with the dynamo extant throughout the convection zone. This concept is consistent with models (e.g., Guerrero et al. 2019), and some detailed MHD models obtain roughly the same power-law index for $P_{cyc}/P_{rot} \propto Ro^\delta$: for example, Warnecke (2018) obtain -0.89 ± 0.04, and if one does a least-squares fit of the five long cycle models in Brun et al. (2022; which are clearly not on the I branch) using their stellar Ro, the slope is -0.90 ± 0.47. These results both compare well with our values of -1.06 ± 0.09 and -0.81 ± 0.17.

We therefore identify the fits found here as representing the initial, more turbulent, α-antiquenched, full convection zone dynamos. Stars on the ZAMS start with rapid rotation, low DR and saturated magnetic activity, likely with predominantly poloidal large-scale field structure (Donati & Landstreet 2009). As stars lose angular momentum, they evolve from the upper right to the lower left in Figure 16, with P_{cyc}/P_{rot} decreasing, and (if Saar 2011 is correct) increasing DR (sketched in Figure 18; red arrows). DR increases to a maximum point, at which point, saturated magnetic activity stops, the α effect starts becoming quenched, and further spindown leads to activity reduction along the well-known rotation-activity relations.

(As a brief aside, we note that an interesting alternative to the full convection zone dynamo, particularly in M stars, is the idea of dynamo cycles driven by thermal fluctuations (e.g., Nigro 2022). This could potentially explain the lack of rotational dependence in M stars, as the distribution of thermal fluctuations would primarily depend on mass/T_{eff}, echoed in the trend seen here of $P_{cyc} \propto \tau$. The similar trend in faster-rotating FGK stars could also be influenced, at least in part, by such a thermally driven dynamo. More work on these models would be useful.)

At some point in partially convective stars, the radiative core and convective envelope decouple (e.g., MacGregor & Brenner 1991), allowing a region of strong shear to form at the interface (the tachocline). The Sun and slower FGK rotators are thought to have $\alpha\Omega$ dynamos with the primary generation region in this strong shear layer. M stars, lacking significant (or any) tachoclines, cannot make this transition.

However, once the tachocline dynamo dominates in older FGK stars, which happens at least by the time the stars reach the I branch around $Ro^{-1} = 1$–3, further cycle evolution proceeds along the I branch, with P_{cyc}/P_{rot} slightly increasing, or may be remaining roughly constant (shown by a blue arrow in Figure 18). Perhaps there is a transitional phase of mixed dynamo dominance before this, explaining the diffuse A branch and the abundance of stars with multiple cycles in this region. The recently noted bend in the chromospheric rotation-activity relation (Lehtinen et al. 2021) may be another reflection of this change. ZDI shows that large-scale toroidal fields already dominate well before the I branch is reached, at around $Ro^{-1} \approx 15$ (on the τ_C scale used here, converted from Donati & Landstreet 2009), about where DR peaks and activity saturation ends (shown by the right dashed magenta line in Figure 18). Perhaps this is where core/envelope decoupling also takes place. Large-scale toroidal field dominance only ends at $Ro^{-1} \approx 2Ro_\odot^{-1} \approx 1$ (Donati & Landstreet 2009)—i.e., at about the time when the star first reaches the I branch. Note that no further stars are seen along the -1.06 slope in Figure 16 among the FGK stars once the I branch is reached. We view this as supporting the final dominance of the tachocline dynamo.

Following the arguments using the same simple dynamo model, Saar & Brandenburg (1999) suggest that the change in slope at the I branch is due to α antiquenching, which implies (surprisingly) that here α increases with the magnetic field ($q_\alpha = 1.10$ on the I branch in Figure 17; Table 3). The reason might be that α in this regime is driven by magnetic buoyancy and pumping effects (Chatterjee et al. 2011). Here again, some detailed MHD models are in reasonably good agreement: a power-law fit to the results of models M1–4 of Warnecke (2018; their slow-moderate rotators, ignoring the very slowest) yields $P_{cyc}/P_{rot} = 213Ro^{0.514}$, which lies between the A and I branches and is of similar slope (shown by the dotted black line in Figure 18). As noted above, we further suggest that some secondary cycles are remnant convection zone dynamos still functioning as the tachocline dynamo ramps up to dominance. This dual P_{cyc}—dual dynamo transitional regime corresponds to the purple transitional epoch arrow in the dynamo evolution in Figure 18.

---

[12] Note: we know of no theoretical or observational motivation for these cycles to have the same period.

Table 3
Model Parameters for $P_{cyc}/P_{rot} = a \times Ro^{-b}$ Models

Stars Included	Stars Excluded	τ	a	σ_a	b	σ_b	RMSE	q_α Unsat.	q_α Sat.	Used in Figures
M	...	G	3.6	1.2	1.02	0.06	0.17	−1.03	1.67	16, 17, 18
FGK	...	G	63.6	1.1	1.06	0.09	0.24	−1.13	1.57	16
I branch	...	G	112.1	1.2	−0.25	0.21	0.13	1.49	...	16
I branch	...	L	101.1	1.1	−0.05	0.24	0.15	1.10	...	17, 18
A branch	...	G	380.3	1.4	−0.15	0.24	0.15	1.30	...	16, 17, 18
A branch	...	G,L[a]	386.3	1.2	−0.12	0.14	0.14	1.25	...	...
FKG	I branch	G	124.0	1.2	0.83	0.11	0.20	−0.67	2.03	...
FKG	A and I branches	G	162.6	1.6	0.81	0.17	0.12	−0.61	2.09	17, 18

Note.
[a] For stars with two cycles, τ_L was used for both if either was on the I branch. The "τ" column denotes the τ we used when estimating convective turnover time (G = global, L = local), the "RMSE" column denotes the root mean square error of the model (in log space), the "Unsat." column gives the q_α value of the model in the unsaturated regime, and the "Sat." column gives the q_α value of the model in the saturated regime.
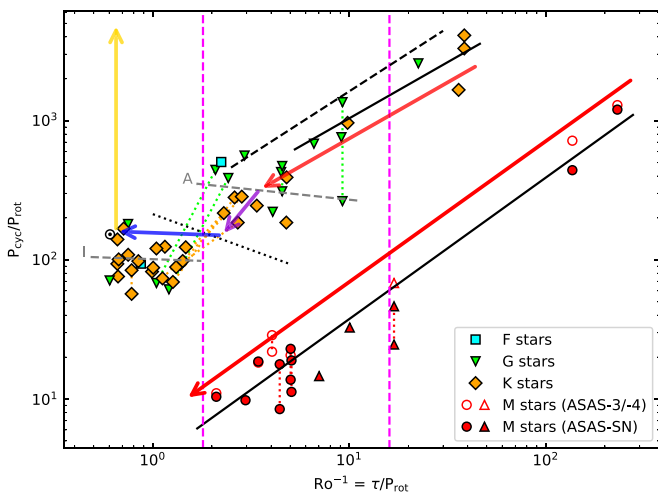
Figure 18. Symbols and gray lines as in Figure 17, with a sketch of the proposed dynamo evolution and MHD model trends overlaid. Evolution begins on the ZAMS at high Ro^{-1} in the upper right corner. Both FGK and M stars begin with α antiquenching α^2 or $\alpha^2\Omega$ dynamos and initially low but increasing DR (red arrows). Core/envelope decoupling in FGK stars (possibly at at a peak in DR and the end of activity saturation; right dashed magenta line) starts a phase of α quenching, and the beginning of the formation of a tachocline, and likely an α antiquenched, tachocline-based $\alpha\Omega$ dynamo as well. This dynamo does not dominate, however, until the star reaches the I branch (blue), although there may be a regime of mixed dynamo dominance first (purple) around the time that large-scale poloidal fields become dominant (left dashed magenta line). After further evolution on the I branch, the star eventually slows to the point that the dynamo sputters, Maunder-like magnetic minima appear, P_{cyc} lengthens, and in the end, the cycle fails entirely, rotational evolution ceases, and the star evolves vertically off the diagram (gold). In M stars, once activity saturation ends (right dashed magenta line), an α-quenched α^2 or $\alpha^2\Omega$ dynamo takes over. 3D MHD models generally agree with the trends found here for the Ms and fast-rotating FGKs (e.g., Brun et al. 2022; dashed black) and the I branch (Warnecke 2018; dotted black). See text for more details.

In the end, however, after further evolution along the I branch, below a critical Ro^{-1}, the dynamo may begin to sputter (van Saders et al. 2016), the star begins to experience magnetic grand minima (Metcalfe et al. 2016), differential rotation weakens (Metcalfe et al. 2022) or may even reverse sign (Gastine et al. 2014; Karak et al. 2020), and the dynamo dies, with P_{cyc} going to infinity (see, e.g., the lengthening P_{cyc} in the evolutionary sequence of G2 stars 18 Sco, the Sun, and α Cen A; Judge et al. 2017). With the cycling dynamo shut down, large-scale fields driving spindown vanish, stopping further

rotational evolution, and the star evolves vertically off the diagram at constant Ro (e.g., Metcalfe & van Saders 2017, shown by a vertical gold arrow in Figure 18).

5. Conclusions

We have found evidence for magnetic activity cycles in at least 12 M-type stars, and traces of cyclic behavior in 3 more, using photometric time series. Of these 15 M dwarfs, approximately 12 are type M3.5 or later and are likely fully convective. For these cycles, we investigated the correlation between cycle amplitude and period, and found that this is reasonably well described by a power law with an exponent of 0.94 ± 0.11. We also found indications of multiple branches in this relation, potentially in agreement with the findings of Saar & Brandenburg (2002). However, the unclear nature of these additional cycles (see Section 3.3) makes the latter less certain.

We further investigated correlations between cycle and rotation period, cycle period and Rossby number, and the ratio of cycle to rotation period and inverse Rossby number. Our results suggest that the dynamo processes acting within M dwarfs may not be as different from those acting in FGK type stars (at least the more rapidly rotating ones with $Ro^{-1} < 3$), as some previous models (e.g., Kitchatinov & Rüdiger 1999) suggest. Some more recent models (e.g., Warnecke 2018; Brun et al. 2022, shown in Figure 18) appear to capture the overall trend for faster-rotating FGK stars in Figure 17; if similar models in fully convective M stars show similar trends, theory and observations may be in reasonable agreement.

Using the Rossby number to parameterize magnetic activity and a simple dynamo model (Saar & Brandenburg 1999), we find that at equivalent Rossby numbers, the α effect is similarly quenched with rotation ($q_\alpha \approx -1$ in the unsaturated regime), but is of reduced amplitude in M dwarfs compared to that of FGK stars. These findings are in agreement with some models (e.g., Ruediger & Kichatinov 1993), but are in apparent disagreement with the results of Saar & Brandenburg (1999), whose limited sample suggested a contrary relation (at least for their A and I branches). However, we propose that what we are actually seeing is the result of one type of dynamo (an α-quenched α^2 or $\alpha^2\Omega$ full convection zone dynamo), present in all fast rotators (a thermally driven dynamo is an alternative possibility). In FGK stars, once they have spun down sufficiently, a tachocline-based α antiquenched $\alpha\Omega$ dynamo takes over (forming the I branch of Brandenburg et al. 1998).

Fully convective M stars, lacking tachoclines, spin down, retaining their full convective zone dynamos. We also find that the α effect is again antiquenched in the saturated regime, which some theoretical models support under certain conditions (e.g., Chatterjee et al. 2011).

Clearly, stellar cycles and the underlying physical mechanisms are not yet fully understood. To follow up this work, we suggest that these stars be monitored using ZDI, which can be used to determine the large-scale magnetic field topology and polarity, and in the UV or X-rays, which are much more sensitive and directly related to magnetic activity. These follow-up observations would reveal whether the cycles presented in Table 1 are a result of global magnetic activity or some other phenomena (i.e., Rossby waves and others). It will be particularly useful to search for more cycles in K7-M2 stars, which are lacking in our sample. These cycles may reveal whether the α effect transition from FGK to fully convective M stars (Figure 16) is sharp or gradual. It is also intriguing that δ (i.e., the power-law slopes) appears to remain constant through the joint α and DR transition when activity saturation ends (Section 4.7); we propose that the implications of this for the underlying dynamo should be explored.

Data Availability

Data analyzed herein are publicly available via the ASAS All-Star Catalog,[14] the ASAS-SN light-curve server,[15] and the Mikulski Space Archive for Space Telescopes (MAST): 10.17909/xdwe-q663. ASAS-4 data on Proxima were provided by G. Pojmański.

---

[13] http://www.astropy.org
[14] http://www.astrouw.edu.pl/asas
[15] https://asas-sn.osu.edu

ORCID iDs

Steven H. Saar ⓘ https://orcid.org/0000-0001-7032-8480
Bradford J. Wargelin ⓘ https://orcid.org/0000-0002-2096-9586
José-Dias do Nascimento, Jr ⓘ https://orcid.org/0000-0001-7804-2145

References

Aigrain, S., Llama, J., Ceillier, T., et al. 2015, MNRAS, 450, 3211
Anthony, F., Núñez, A., Agüeros, M. A., et al. 2022, AJ, 163, 257
Astudillo-Defru, N., Díaz, R. F., Bonfils, X., et al. 2017, A&A, 605, L11
Astropy Collaboration, Price-Whelan, A. M., Sipőcz, B. M., et al. 2018, AJ, 156, 123
Astropy Collaboration, Robitaille, T. P., Tollerud, E. J., et al. 2013, A&A, 558, A33
Babcock, H. D. 1959, ApJ, 130, 364
Babcock, H. W. 1961, ApJ, 133, 572
Baliunas, S., Frick, P., Moss, D., et al. 2004, SoPh, 224, 179
Baliunas, S. L., Donahue, R. A., Soon, W. H., et al. 1995, ApJ, 438, 269
Baluev, R. V. 2008, MNRAS, 385, 1279
Baraffe, I., & Chabrier, G. 2018, A&A, 619, A177
Barnes, J. R., Collier Cameron, A., Donati, J. F., et al. 2005, MNRAS Lett., 357, L1
Basri, G. 2018, ApJ, 865, 142
Böhm-Vitense, E. 2007, ApJ, 657, 486
Bonfils, X., Delfosse, X., Udry, S., et al. 2013, A&A, 549, A109
Boro Saikia, S., Marvin, C. J., Jeffers, S. V., et al. 2018, A&A, 616, A108
Brandenburg, A., Saar, S. H., & Turpin, C. R. 1998, ApJL, 498, L51
Brasseur, C. E., Phillip, C., Fleming, S. W., Mullally, S. E., & White, R. L. 2019, Astrocut: Tools for creating cutouts of TESS images, Astrophysics Source Code Library, ascl:1905.007
Brun, A. S., Strugarek, A., Noraz, Q., et al. 2022, ApJ, 926, 21
Chabrier, G., & Baraffe, I. 1997, A&A, 327, 1039
Charbonneau, P. 2010, LRSP, 7, 3
Chatterjee, P., Mitra, D., Rheinhardt, M., & Brandenburg, A. 2011, A&A, 534, A46
Claytor, Z. R., van Saders, J. L., Llama, J., et al. 2022, ApJ, 927, 219
Coppenbarger, D. S., Henry, T. J., & McCarthy, D. W. J. 1994, AJ, 107, 1551
Corsaro, E., Bonanno, A., Mathur, S., et al. 2021, A&A, 652, L2
Cuntz, M., Rammacher, W., Ulmschneider, P., Musielak, Z. E., & Saar, S. H. 1999, ApJ, 522, 1053
Damasso, M., Del Sordo, F., Anglada-Escudé, G., et al. 2020, SciA, 6, eaax7467
Davenport, J. R. A., Mendoza, G. T., & Hawley, S. L. 2020, AJ, 160, 36
Davison, C. L., White, R. J., Henry, T. J., et al. 2015, AJ, 149, 106
Deming, D., Knutson, H., Kammer, J., et al. 2015, ApJ, 805, 132
Dikpati, M., & Charbonneau, P. 1999, ApJ, 518, 508
Distefano, E., Lanzafame, A. C., Lanza, A. F., Messina, S., & Spada, F. 2017, A&A, 606, A58
Donahue, R. A., & Baliunas, S. L. 1992, SoPh, 141, 181
Donahue, R. A., Saar, S. H., & Baliunas, S. L. 1996, ApJ, 466, 384
Donati, J. F., & Landstreet, J. D. 2009, ARA&A, 47, 333
Durney, B. R., De Young, D. S., & Roxburgh, I. W. 1993, SoPh, 145, 207
Feiden, G. A., Skidmore, K., & Jao, W.-C. 2021, ApJ, 907, 53
Gastine, T., Duarte, L., & Wicht, J. 2012, A&A, 546, A19
Gastine, T., Yadav, R. K., Morin, J., Reiners, A., & Wicht, J. 2014, MNRAS Lett., 438, L76
Gatewood, G., Coban, L., & Han, I. 2003, AJ, 125, 1530
Gilman, P. A. 1969, SoPh, 8, 316
Gilman, P. A., & Fox, P. A. 1997, ApJ, 484, 439
Ginsburg, A., Sipőcz, B. M., Brasseur, C. E., et al. 2019, AJ, 157, 98
Guerrero, G., Zaire, B., Smolarkiewicz, P. K., et al. 2019, ApJ, 880, 6
Hale, G. E. 1908, ApJ, 28, 315
Hale, G. E. 1913, ApJ, 38, 27
Hale, G. E., Ellerman, F., Nicholson, S. B., & Joy, A. H. 1919, ApJ, 49, 153
Harris, C. R., Millman, K. J., van der Walt, S. J., et al. 2020, Natur, 585, 357
Henry, T. J., Franz, O. G., Wasserman, L. H., et al. 1999, ApJ, 512, 864
Hébrard, É. M., Donati, J. F., Delfosse, X., et al. 2016, MNRAS, 461, 1465
Hunter, J. D. 2007, CSE, 9, 90
Ibañez Bustos, R. V., Buccino, A. P., Messina, S., Lanza, A. F., & Mauas, P. J. D. 2020, A&A, 644, A2
Jao, W.-C., Couperus, A. A., Vrijmoet, E. H., Wright, N. J., & Henry, T. J. 2022, ApJ, 940, 145

Jao, W.-C., Henry, T. J., Gies, D. R., & Hambly, N. C. 2018, ApJL, 861, L11
Jenkins, J. M., Twicken, J. D., McCauliff, S., et al. 2016, Proc. SPIE, 9913, 99133E
Judge, P. G., Egeland, R., Metcalfe, T. S., Guinan, E., & Engle, S. 2017, ApJ, 848, 43
Judge, P. G., Solomon, S. C., & Ayres, T. R. 2003, ApJ, 593, 534
Käpylä, P. J. 2021, A&A, 651, A66
Käpylä, P. J., Mantere, M. J., & Brandenburg, A. 2013, GApFD, 107, 244
Karak, B. B., Tomar, A., & Vashishth, V. 2020, MNRAS, 491, 3155
Kent, S. M. 1985, PASP, 97, 165
Kervella, P., Arenou, F., Mignard, F., & Thévenin, F. 2019, A&A, 623, A72
Kővári, Z., Frasca, A., Biazzo, K., et al. 2011, in IAU Symp. 273, The Physics of Sun and Star Spots, Vol. 273, ed. D. Prasad Choudhary & K. G. Strassmeier (Cambridge: Cambridge Univ. Press), 121
Kitchatinov, L. L., & Rüdiger, G. 1999, A&A, 344, 911
Kochanek, C. S., Shappee, B. J., Stanek, K. Z., et al. 2017, PASP, 129, 104502
Kovári, Z., Strassmeier, K. G., Granzer, T., et al. 2004, A&A, 417, 1047
Krishnamurthi, A., Terndrup, D. M., Pinsonneault, M. H., et al. 1998, ApJ, 493, 914
Landin, N. R., Mendes, L. T. S., Vaz, L. P. R., & Alencar, S. H. P. 2023, MNRAS, 519, 5304
Lehmann, L. T., Künstler, A., Carroll, T. A., & Strassmeier, K. G. 2015, AN, 336, 258
Lehtinen, J., Jetsu, L., Hackman, T., Kajatkari, P., & Henry, G. W. 2016, A&A, 588, A38
Lehtinen, J. J., Käpylä, M. J., Olspert, N., & Spada, F. 2021, ApJ, 910, 110
Leighton, R. B. 1969, ApJ, 156, 1
Lightkurve Collaboration, Cardoso, J. V. d. M., Hedges, C., et al. 2018, Lightkurve: Kepler and TESS time series analysis in Python, Astrophysics Source Code Library, ascl:1812.013
Lomb, N. R. 1976, Ap&SS, 39, 447
Luger, R., Agol, E., Kruse, E., et al. 2016, AJ, 152, 100
Luger, R., Kruse, E., Foreman-Mackey, D., Agol, E., & Saunders, N. 2018, AJ, 156, 99
MacGregor, K. B., & Brenner, M. 1991, ApJ, 376, 204
Metcalfe, T. S., Egeland, R., & van Saders, J. 2016, ApJL, 826, L2
Metcalfe, T. S., Finley, A. J., Kochukhov, O., et al. 2022, ApJL, 933, L17
Metcalfe, T. S., & van Saders, J. 2017, SoPh, 292, 126
Montesinos, B., Thomas, J. H., Ventura, P., & Mazzitelli, I. 2001, MNRAS, 326, 877
Moré, J. J. 1978, Lecture Notes in Mathematics, Vol. 630 (Berlin: Springer Verlag), 105
Mortier, A. 2016, in 19th Cambridge Workshop on Cool Stars, Stellar Systems, and the Sun (Zenodo), 134
Nigro, G. 2022, ApJ, 938, 22
Noyes, R. W., Weiss, N. O., & Vaughan, A. H. 1984, ApJ, 287, 769

O'dell, M. A., Panagi, P., Hendry, M. A., & Collier Cameron, A. 1995, A&A, 294, 715
Olspert, N., Lehtinen, J. J., Käpylä, M. J., Pelt, J., & Grigorievskiy, A. 2018a, A&A, 619, A6
Olspert, N., Pelt, J., Käpylä, M. J., & Lehtinen, J. 2018b, A&A, 615, A111
Ossendrijver, M. 2003, A&ARv, 11, 287
Parker, E. N. 1955, ApJ, 121, 491
Pecaut, M. J., & Mamajek, E. E. 2013, ApJS, 208, 9
Pojmanski, G. 1997, AcA, 47, 467
Pojmanski, G. 2002, AcA, 52, 397
Reiners, A. 2012, LRSP, 9, 1
Rieger, E., Share, G. H., Forrest, D. J., et al. 1984, Natur, 312, 623
Robinson, R. D., & Durney, B. R. 1982, A&A, 108, 322
Rüdiger, G., Elstner, D., & Ossendrijver, M. 2003, A&A, 406, 15
Ruediger, G., & Kichatinov, L. L. 1993, A&A, 269, 581
Saar, S. H. 2011, in IAU Symp. 273, The Physics of Sun and Star Spots, ed. D. Prasad Choudhary & K. G. Strassmeier (Cambridge: Cambridge Univ. Press), 61
Saar, S. H., & Brandenburg, A. 1999, ApJ, 524, 295
Saar, S. H., & Brandenburg, A. 2002, AN, 323, 357
Saar, S. H., Buente, M., & Solanki, S. K. 1994, in ASP Conf. Ser. 64, Cool Stars, Stellar Systems, and the Sun, ed. J.-P. Caillault (San Francisco, CA: ASP), 474
Scargle, J. D. 1982, ApJ, 263, 835
Schwabe, H. 1844, AN, 21, 233
Shappee, B. J., Prieto, J. L., Grupe, D., et al. 2014, ApJ, 788, 48
Suárez Mascareño, A., Rebolo, R., & González Hernández, J. I. 2016, A&A, 595, A12
Suárez Mascareño, A., Rebolo, R., González Hernández, J. I., & Esposito, M. 2015, MNRAS, 452, 2745
Tobias, S. M. 1998, MNRAS, 296, 653
Toriumi, S., & Park, S.-H. 2022, arXiv:2204.06010
van Saders, J. L., Ceillier, T., Metcalfe, T. S., et al. 2016, Natur, 529, 181
van Saders, J. L., & Pinsonneault, M. H. 2012, ApJ, 751, 98
Vilhu, O. 1984, A&A, 133, 117
Virtanen, P., Gommers, R., Oliphant, T. E., et al. 2020, NatMe, 17, 261
Vrijmoet, E. H., Henry, T. J., Jao, W.-C., & Dieterich, S. B. 2020, AJ, 160, 215
Waldmeier, M. 1935, Mitt. Eidgen. Sternw. Zurich, 14, 105
Wargelin, B. J., Saar, S. H., Pojmański, G., Drake, J. J., & Kashyap, V. L. 2017, MNRAS, 464, 3281
Warnecke, J. 2018, A&A, 616, A72
Wilson, O. C. 1978, ApJ, 226, 379
Windhorst, R. A., Burstein, D., Mathis, D. F., et al. 1991, ApJ, 380, 362
Winters, J. G., Henry, T. J., Jao, W.-C., et al. 2019, AJ, 157, 216
Wright, N. J., Drake, J. J., Mamajek, E. E., & Henry, G. W. 2011, ApJ, 743, 48
Wright, N. J., Newton, E. R., Williams, P. K. G., Drake, J. J., & Yadav, R. K. 2018, MNRAS, 479, 2351